# Metal Organic Framework (MOF) Derived Nanostructured Composite @ Reduced Graphene Oxide as an Efficient Electrocatalyst for Oxygen Reduction Reactions


**By**

**M. Asad Ali**

**Reg. No 00000320519**

**Supervised by**
**Dr. Naseem Iqbal**

**US-Pakistan Center for Advanced Studies in Energy (USPCAS-E)**

**National University of Sciences and Technology (NUST)**

**H-12, Islamabad 44000, Pakistan**


**March 2022**

# Metal Organic Framework (MOF) Derived Nanostructured Composite @ Reduced Graphene Oxide as an Efficient Electrocatalyst for Oxygen Reduction Reactions


**By**

**M. Asad Ali**

**Reg. No 00000320519**
**Session 2019-2021**

**Supervised by**
**Dr. Naseem Iqbal**


**A Thesis Submitted to the US-Pakistan Center for Advanced Studies in Energy in partial fulfillment of the requirements for the degree of Master of Science in Energy Systems Engineering**


**US-Pakistan Center for Advanced Studies in Energy (USPCAS-E)**

**National University of Sciences and Technology (NUST)**

**H-12, Islamabad 44000, Pakistan**


**March 2022**

## THESIS ACCEPTANCE CERTIFICATE

Certified that final copy of MS/MPhil thesis written by **Mr. M. Asad Ali, (Registration No. 00000320519)**, of U.S Pakistan Center for Advanced Studies in Energy has been vetted by undersigned, found complete in all respects as per NUST Statues/Regulations, is within the similarity indices limit and is accepted as partial fulfillment for the award of MS/MPhil degree. It is further certified that necessary amendments as pointed out by GEC members of the scholar have also been incorporated in the said thesis.

Signature: _____

Name of Supervisor: Prof. Dr. Naseem Iqbal

Date: _____

Signature (HoD): _____

Date: _____

Signature (Dean/Principal): _____

Date: _____

# Certificate

This is to certify that work in this thesis has been carried out by **Mr. M. Asad Ali** and completed under my supervision in Energy Conservation and Storage laboratory, US-Pakistan Center for Advanced Studies in Energy (USPCAS-E), National University of Sciences and Technology, H-12, Islamabad, Pakistan.

Supervisor:

Prof. Dr. Naseem Iqbal
USPCAS-E
NUST, Islamabad

GEC member 1:

Dr. Nadia Shahzad
USPCAS-E
NUST, Islamabad

GEC member 2:

Dr. Mustafa Anwar
USPCAS-E
NUST, Islamabad

GEC member 3:

Dr. Ghulam Ali
USPCAS-E
NUST, Islamabad

HOD-ESE:

Dr. Rabia Liaquat
USPCAS-E
NUST, Islamabad

Dean/Principal:

Prof. Dr. Adeel Waqas
USPCAS-E
NUST, Islamabad

# Acknowledgements

All praise to the great Allah Almighty who has bestowed me with the opportunity to seek knowledge and enabled me to fulfill the obligation to explore the world of science up to my maximum limits.

I would like to express my sincere gratitude to my research supervisor **Prof. Dr. Naseem Iqbal** for his motivation, continuous support, patience and immense knowledge. He has guided me completely through-out my research work. Working under his supervision has indeed broadened my vision.

I am also really thankful to my GEC members: **Dr. Nadia Shahzad; Dr. Ghulam Ali and Dr. Mustafa Anwar** for sparing precious time from their busy schedules, for suggestions as well as moral support besides this I would like to thank the USPCASE faculty for being extremely cooperative.

A special thanks to lab engineers at Synthesis lab, Biofuel lab, AEMS lab and Combined lab **Eng. Muhammad Naveed Ahmad, Eng. Ali Abdullah, Eng. Asghar Ali, Eng. Aamir Satti and Qamar-ud-Din** who helped me a lot in the experimental work and testing.

Last but not the least, I would pay my regards to my family for their un-parallel love, support and encouragement throughout my research work and my friends and seniors, Abdul Wahab, Muhammad Umair Imtiaz, Awais Ahmad, Nisar Ahmed, Muhammad Zain and Muhammad Arslan Raza to accompany me in this journey.

Regards,

**M. Asad Ali**

# Dedication

*Dedicated to my exceptional parents and adored siblings whose tremendous support and cooperation led me to this wonderful accomplishment.*

# Abstract

Energy storage devices have the potential to play a significant part in the restructuring of the energy sector by delivering an inexpensive, accessible, and reliable source of energy directly at the point of demand while likewise reducing the load on the central power grid. Due to their limited energy densities and capacities, lithium-ion batteries (LIBs) are considered inadequate to address expanding energy storage demands. Metal air batteries (particularly Li-air batteries) are a relatively new technology that has gained attention due to its potentially high energy densities and novel cell designs. When it comes to the oxygen reduction reactions that underlie the processes during discharge and charge cycles, poor electrocatalyst materials severely affect the impressive theoretical energy densities of Li-air batteries (LABs), which is roughly twenty times the density of commercial Li-ion batteries (LIBs). To solve its performance difficulties, a electrocatalyst that is efficient, stable, and long-lasting is required. A manganese metal organic framework and graphene oxide nanostructured composite was prepared in this study using a simple solvothermal approach followed by thermal reduction in an inert atmosphere. One nanostructured composite with 30% rGO (MnBDC@30% rGO) excels the majority of recently described catalysts in terms of electrocatalytic property and electroactivity. Electrochemical tests of Mn/Zn-N-C @30% rGO show significant cathodic peak potentials, onset, and half wave, as well as acceptable current densities. It exhibits excellent ORR performance in terms of low overpotential, material degradation, high methanol tolerance, and long-term stability, which can be attributed to a synergistic effect between the mesoporous and highly defective catalyst surface, as well as the transition metal organic framework and rGO chemistries.

**Key Words:** *Oxygen reduction reaction, metal organic framework, reduced graphene oxide, mesoporous*

# Table of Contents

# List of Figures

# List of Tables

# Publications

**Asad Ali**, Naseem Iqbal, Tayyaba Noor, Umair Imtiaz, **"Nanostructured Mn-doped Zn-N-C @reduced graphene oxide as high performing electrocatalyst for oxygen reduction reaction"** (Under-Review in Journal of Electroanalytical Chemistry)

# List of Abbreviations/Nomenclature

| | |
|---|---|
| rGO | Reduced Graphene Oxide |
| XRD | X-Rays Diffraction |
| SEM | Scanning Electron Microscopy |
| TGA | Thermogravimetric Analysis |
| BET | Braunner Emmett Teller |
| EDS | Energy Dispersive X-ray Spectroscopy |
| LIB | Lithium-Ion Battery |
| MAB | Metal Air Battery |
| ORR | Oxygen Reduction Reaction |
| CP | Chronopotentiometry |
| LSV | Linear Sweep Voltammetry |
| CV | Cyclic Voltammetry |
| EIS | Electrochemical Impedance Spectroscopy |
| MOF | Metal Organic Frame Works |
| ZIF | Zeolitic Imidazolate Framework |
| ESS | Energy Storage System |
| SHE | Standard Hydrogen Electrode |

# CHAPTER 1

# Introduction

## 1.1 Global Energy Demand Scenario

With the introduction of energy and power in economic and social spheres, modern civilizations have undergone revolutionary transformations. Today, industrial growth determines a nation's economy and well-being. Industries rely significantly on an uninterrupted supply of inexpensive and dependable power. As long as there is a consistent supply of power to the industrial sector, economic development and business flourishing are ensured, results in the transformation of society into a more autonomous and stable state. So, a continuous supply of energy must be assured for struggling economies in order to address the problems of sustainable development [1].

Environmental pollution appears to be generating existential problems all around the world, and it has gotten more attention in the recent years because of the ticking time bomb which is global warming. Environmental pollution has the potential to endanger human existence on the planet. Because of their unpredictable market circumstances, diminishing nature of resources, and carbon pollution, non-renewable fossil fuels have generated major problems for emerging economies. Non-renewable sources of energy cannot be considered as a reliable source of energy since they impede sustainable development and do not promise to address long-term progress issues. As a result, an energy transition from fossil fuels to renewable energy is occurring gradually in the power sector, and every developing country is attempting to explore indigenous energy resources in order to mitigate the economic insecurity associated with fossil fuels while also achieving environmental protection goals set forth in international forums. By 2020, renewable energy accounted for 28% of the worldwide energy mix, with hydroelectric energy accounting for the largest share, while other renewable sources accounted for just 5% of power generation [2, 1].

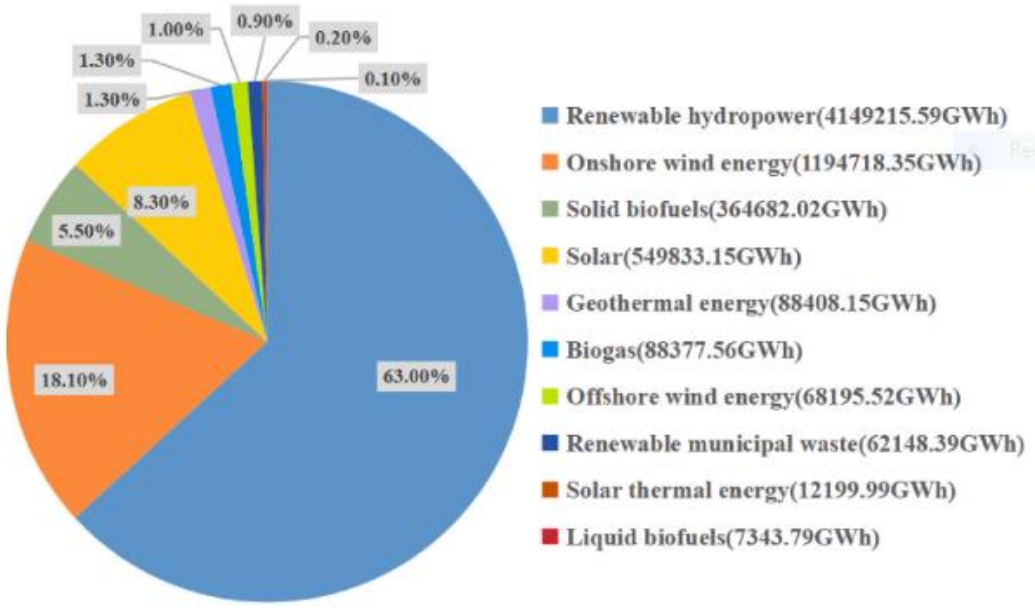


***Fig. 1. 1:*** Proportion Current Worldwide Energy Usage from Renewables [3]

## 1.2 Pakistan's Energy Outlook

As a developing country, Pakistan, by 2018, had a population of 212.2 million. Pakistan's energy usage per capita is relatively low in comparison to other countries, with about 460.3 Kilograms oil equivalent. In contrast, it is less than 50% of developing nations, 24% of the worldwide average, approximately 11% of the overall average of Organization for Economic Cooperation and Development (OECD) member countries, and 5% of the developed world [4, 5] According to a recent Asian Development Bank research, low energy consumption in Pakistan is attributed to insufficient local energy supply [6]. But overall energy consumption in Pakistan has shown progressive upward trends and in the next decades, like many developing countries, it is predicted that this trend in consumption would be followed.

It is projected that power demand will increase in the next decade based on the present energy consumption pattern. According to Qasim et al., the rate of growth in energy consumption was estimated to be 8% in the first decade of this century, and it is expected to continue to rise, escalating the energy problem [7]. During the next several years, demand is anticipated to increase at a pace of 8-10% each year, reaching 54,000

megawatts (MW) in 2020. If the current trend continues, it is expected to reach 113,000 MW by 2030. Rural development and uplift programmes, suburban urbanization, government commitments to electrify remote and underserved areas, expansion of the agricultural, industrial, and service sectors, planned development of new residential and economic zones, and adoption of modern machinery and appliances with little or no energy-saving attributes are just a few of the factors that will noticeably impact the future. The government should take advantage of this situation to mainstream alternative and renewable sources of energy while also investing in the promotion and development of contemporary power generating technologies in order to prevent an impending energy crisis from derailing long-term development. Fig 1.2 depicts Pakistan's current and anticipated electricity consumption trends from 2010 to 2040.

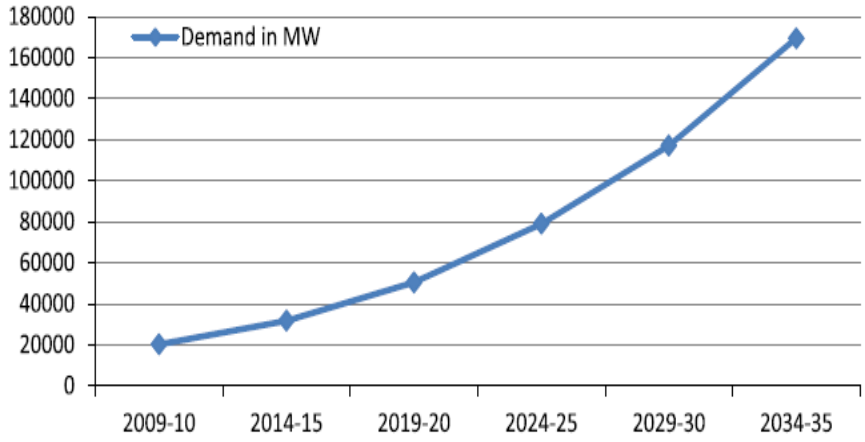


***Fig. 1.2:*** Pakistan's projected trend in electricity demand from 2010 to 2035 [8].

## 1.3 Power generation from available sources in Pakistan

Primary energy supply in Pakistan is dominated by fossil fuels, which account for the majority of the overall energy mix. They are used to generate thermal energy, which is used to heat homes and businesses. Oil and Gas grab 81% of the diagram, while coal makes up a measly 5%. According to 2014 statistics, renewable energy sources such as hydropower and nuclear provide up to 14% of the national energy mix. Similarly, the fossil fuels again contribute mainly to the electricity generating sector, representing 61% of the pie chart. It is powered by hydroelectricity production, which accounts for 33% of the total capacity. A total of 5.6 percent of the power sector's energy comes from nuclear

and other sources of power production A small portion of the national power system is powered by wind energy, although it only makes up 0.2% of the total [9].

Due to difficult economic circumstances, Pakistan's topography is of special strategic significance, and the country's vast renewable natural resources remain mostly unexplored. It is possible to harness renewable energy sources such as biomass, wind, sun, and modest hydropower with the help of government assistance. Recently, a number of projects to harness the country's renewable energy resources have been created, while others are now in the development phase. In recent years, many renewable energy projects have been built and are now operating in capacity, including wind, solar, micro hydro, and bagasse-based powerplants, with installed capacities ranging from 308 megawatts (MW), 100 megawatts (MW), 145 megawatts (MW), 98 megawatts (MW), respectively. In addition to the projects completed, some projects are presently under development and are projected to complete 4,931 MW of additional generating capacity. These include 856 MW of solar, 1140 MW of wind and bagasse, and 2638 MW of water-based power. Once these projects are completed, the gap between demand and supply is anticipated to close.

The energy deficit is replaced by energy surplus, and the demand-supply balance is controlled. Electric energy storage devices will become more important in the future years. In this context, it is worthwhile to examine the significance of energy storage in reducing energy losses and supplying energy during peak demand periods. In addition, EES alternatives that may support power generators should be briefly reviewed.

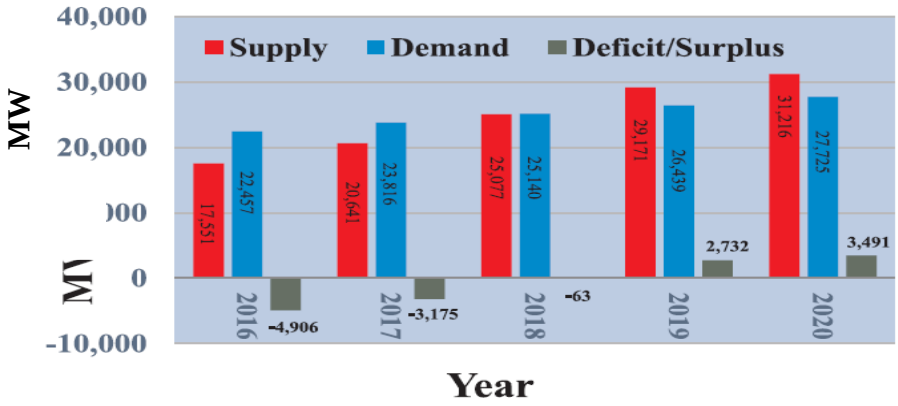


***Fig. 1. 3:*** Changes in demand and supply during recent [10]

## 1.4 Role of Energy Storage in renewable energy generation systems

In order to meet increasing demand for energy and environmental safety, energy storage from green and renewable sources of energy production has been seen as a realistic alternative for continuous provision of high-quality electricity in times of uneven demand. Although energy generated from renewable resources is clean and green, the nature of production is unstable and unpredictable due to its reliance on weather conditions, geological resource placement, season fluctuation, and power system efficiency. These inevitable factors cause variations in power production, making it useless for dependable power delivery. Integrating energy storage devices into the electric energy and storing as much power as possible during peak use hours is the best option for these somewhat unpredictable systems [11, 12].

In addition, these electrical storage systems (EES) offer additional advantages in terms of voltage maintenance, frequency control and load management in times of surplus electricity energy [13]. Green energy collected from ecologically friendly sources may be maintained as high-quality electricity and made available whenever it is required in this manner. Figure 1.4 depicts a general trend in energy demand and supply in a typical grid electrical supply, as well as the effect of EES on reducing the imbalance between electricity demand and consumption [12].

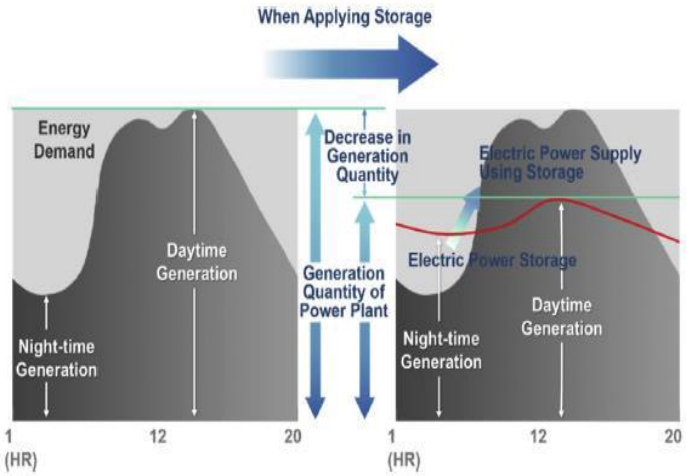


***Fig. 1. 4:*** EES's role in power load levelling [13]

## 1.5 Overview of different electrochemical energy storage systems

### 1.5.1 Electrochemical Energy Storage

Chemical reactions in batteries convert the chemical energy of redox species into electrical energy, which is stored in batteries. Batteries are electrochemical storage devices. Every battery system, in its most basic form, comprises of an anode, a cathode, and an electrolyte. Oxidation and reduction processes occur at the anode and cathode, respectively, with the electrolyte facilitating ionic mobility for these reactions. Between the electrodes, a separator is inserted to avoid physical contact between the electrodes and the permeate ions. Different battery systems are developed utilizing various electrode combinations, resulting in numerous choices accessible depending on application. If you are looking for an appropriate battery, you should take into account factors such as cost, energy and power output, cycle life, and depth of discharge.

The lithium-ion battery is now the most popular kind of battery used in electronic applications because of its long life and durability. LIBs, on the other hand, have a very high cost of energy storage for stationary power applications, averaging about $1000/kWh. When it comes to integrating high energy density devices into existing power systems, the cost of LIBs is one of the most important issues that must be addressed immediately. We'll go through the many types of rechargeable batteries, how they work, and what characteristics they have that are related to energy battery.

#### 1.5.1.1 Fuel Cell

Hydrogen and oxygen are exchanged between the anode and cathode of a fuel cell in order to produce electricity. Fuel cells also produce heat through the process of releasing chemical energy from other fuels and converting it to electricity. The anode produces electrons and protons from hydrogen molecules. Protons can move through an electrolyte membrane while electrons must move through a circuit. This creates an electric current and extra heat, as well as a lot of electricity. When protons, electrons, and oxygen mix at

the cathode, water molecules are produced. Fig 1.5 shows a fuel cell energy storage and conversion device in logical order.

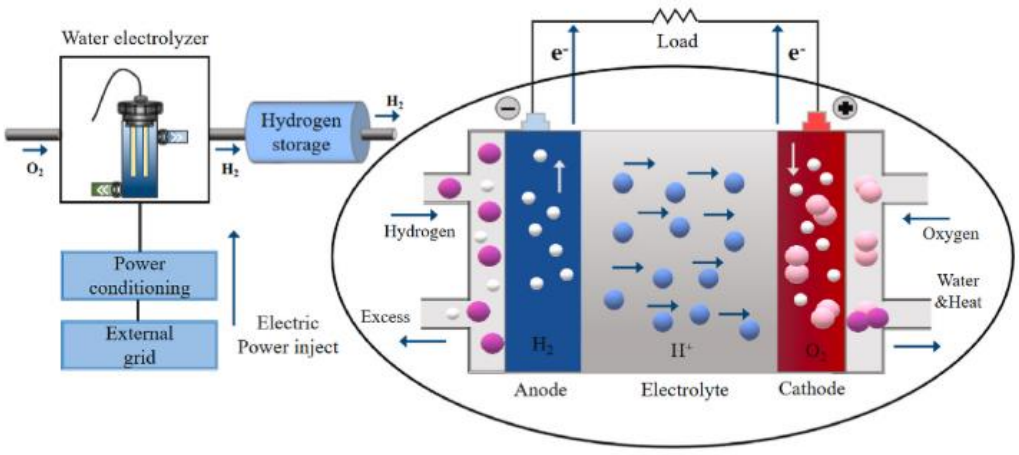


***Fig. 1.5:*** Schematic diagram of fuel cell system

**1.5.1.2 Post Lithium-ion (Metal-Air) battery Systems:**

There are several disadvantages associated with currently utilized batteries resulting from the material chemistry and electrochemical reaction mechanisms that occur inside the batteries. Most commercial batteries are affected by low energy density, short cyclical life and low voltage due to inadequate electrical energy densities and electrocatalytic capabilities of electrodes. This weakness has led to novel battery designs and chemicals that can guarantee a maximum energy density of double, high initial discharge capacity, high nominal voltages and a reliable function. The current generation of LIBs evolved from lithium metal batteries, which utilized a highly reactive lithium metal anode. However, this concept was not practical so that scientists substituted lithium anode with graphite, which accommodates lithium ions originating from lithium intercalated cathode. This design was based on the storage and extraction of high energies from lithium metal. This allowed scientists to use undiscovered lithium potential.

LIBs are not suitable for large-scale use in power systems owing to their high cost and safety risks. There is a lot of research under way in the development of new battery chemistries that have inherent energy and power density, faster charging/discharge capacity, longer life and low costs, environmental and operational safety. With potential

energy density of lithium metal approaching gasoline, major research is undertaken to create lithium batteries of the next generation. In this field, two battery concepts are being actively researched: lithium metal batteries and lithium air batteries. Lithium battery utilizes lithium metal anode and porous air cathode, as the title says. The anode serves as a source of lithium and sheds electrons after suffering oxidation during discharge, while the cathode is intended to electrochemically reduce oxygen to create and temporarily store discharge products. Air cathode design is important for success and electrochemical performance since it affects how quickly kinetics progress and reversible product discharge is generated. Here, we will briefly discuss the lithium air batteries to provide an overview of its competitive edge over other battery systems and how our research can help to develop a valuable storage system.

#### 1.5.1.3 Lithium Air Batteries

Metal-air batteries are gaining popularity as a result of their efficient conversion and storage capacities, ecologically friendly techniques, and distinctive open cell designs. Metal-air batteries theoretically have energy densities about three to thirty times that of conventional lithium-ion batteries (LIBs). Since LIB has almost reached its theoretical limit of performance it must be hypothetically replaced by more energy-dense storage devices and metal-air batteries, it seems to be a fine replacement for LIBs.

There are many metal air battery types, but those based on lithium (Li), sodium (Na), magnesium (Mg), potassium (K), aluminium (Al), iron (Fe), and zinc (Zn) are of special importance. In this class of electrochemical storage devices, Li-air and Zn-air are the two most notable members. Due to the scarcity of resources, Li-air has a very high theoretical energy density (11,429 Wh $kg^{-1}$), specific capacity (3,860 $mAhg^{-1}$), and cell voltage (2.96V). While zinc-air batteries, with their relatively high theoretical energy density (1,350 W h $kg^{-1}$), are abundant in low-cost materials. So a compromise between production cost and energy recovery is required here. Because Li-air batteries have a similar capacity to gasoline (13,000 W h $kg^{-1}$), they may be used as an alternative for fossil fuels in electric or plug-in cars (EVs and PHEVs). However, the full potential of these systems is challenging to realize owing to underlying design, operating and chemistry issues. Fig. 1.6 shows a comparison of theoretical energy densities for lead acid, sodium

Sulphur, lithium ion, vanadium redox flow, zinc-air, and lithium-air battery systems. Li-air outperforms all other systems due to its extraordinarily high values, which make it suitable for use in power systems and automobile applications [14, 15].

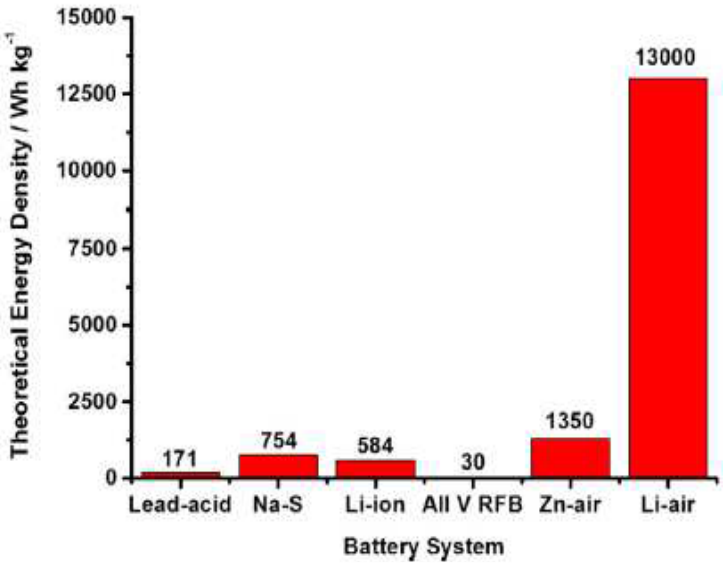


***Fig. 1. 6:*** Comparison of theoretical energy densities of rechargeable batteries [15]

## 1.6 Oxygen electrocatalysis (Oxygen reduction and evolution)

Li-air batteries use oxygen electrocatalysis to store and release energy during charging/discharging cycles. Gas diffusion electrode (also known as air electrode) is affected, increasing its significance in determining cell's electrochemical performance. During the discharge process, an oxygen reduction reaction (ORR) actually took place at the cathode, mixing lithium ions and electrons using oxygen gas molecules that are being introduced. The discharge product is largely reliant on the reaction kinetics of the electrolyte as well as the solvate characteristics of the solution. It is discovered that the production of $Li_2O$ results in a high energy density of 5280 W h $kg^{-1}$ when the charge transfer number is 4. However, this product is shown to be thermodynamically unstable. $Li_2O_2$ is a common discharge product that collects around the porous air cathode, providing a potential energy density of 3500 W h $kg^{-1}$.

Half-cell reactions taking place inside a Li-air battery have been shown below:
Anodic half-cell reaction:

$$Li \rightleftharpoons Li^{+} + e^{-} \qquad \text{eq. (1.13)}$$

Cathodic half-cell reaction:

$$O_2 + e^{-} \rightleftharpoons O_2{}^{-} \qquad \text{eq. (1.14)}$$

$$O_2{}^{-} + Solvent \rightleftharpoons (Solvent - O_2)^{-} \qquad \text{eq. (1.15)}$$

$$(Solvent - O_2)^{-} + Li^{+} \rightleftharpoons O_2{}^{-} - Li^{+}(Solvent)_n \qquad \text{eq. (1.16)}$$

$$LiO_2 + Li^{+} + e^{-} \rightleftharpoons Li_2O_2 \qquad \text{eq. (1.17)}$$

$$Li_2O_2 + 2Li^{+} + 2e^{-} \rightleftharpoons 2Li_2O \qquad \text{eq. (1.18)}$$

When ORR begins, the reactant oxygen molecule is reduced first into an anionic molecular radical, which is then solvated into an electrolyte solution and reacts with lithium ions to create lithium superoxide. On receiving an electron, lithium superoxide transforms into lithium peroxide. Lithium peroxide is reduced to lithium oxide via a series of steps. This process is attributed to $4e^-$ transfer because each $Li_2O$ molecule needs four electrons to form. It is advantageous to use non-aqueous electrolytes including lithium air cells because they provide an inherent solid electrolyte interface barrier that does not need the use of an additional protective layer. It is important that the insoluble discharge product that is kept within the porous material framework during the charging process be fully reversible. In non-catalytic natural circumstances, ORR happen extremely slowly. To ensure the long-term stability, battery, and performance of lithium air batteries, a high-performance electrocatalyst material is almost always needed to help the ORR reaction.

## 1.7 Challenges and limitation in oxygen electrocatalysis

Despite the fact that lithium air batteries offer amazingly high specific energy densities, there are a number of issues that impede their commercialization. These issues create numerous flaws in the regular and dependable functioning of batteries, which must be addressed. These are the issues:

1. Extremely high overpotentials while charging and discharging
2. In contrast to theoretical values, discharge capacities are low.
3. Inadequate capacity retention
4. There is a short cyclic existence.

If we probe further, we'll find that these problems are caused by poor electrochemical and material characteristics of various cell components. More precisely, reaction kinetics, material stability, bifunctional abilities, surface and morphological characteristics all have a significant impact on cell activity. The electrocatalyst material in a lithium air battery must impart extremely rapid reaction kinetics so that ORR and OER may occur more often. Unfortunately, no materials that can guarantee optimal performance has yet been marketed. There are many reasons for poor battery performance include sluggish reaction kinetics, deterioration of catalyst materials, blockage of pores containing discharge product, and corrosion of electrolyte.

The majority of battery problems are intricately linked to the electrocatalyst material's characteristics. The following are desirable characteristics of an electrocatalyst for a lithium air battery:

1. High reaction kinetics for ORR
2. Serve as a discharge product reservoir
3. Reversible product deposition
4. Porosities that are bimodal (meso + macro)
5. Conductivity of electrons
6. Increased cycle life and capacity.

In order to fabricate the battery systems, we want, it is critical to create materials with the characteristics listed above and utilize them in the fabrication process. Thesis breakdown steps are shown in Fig. 1.7.

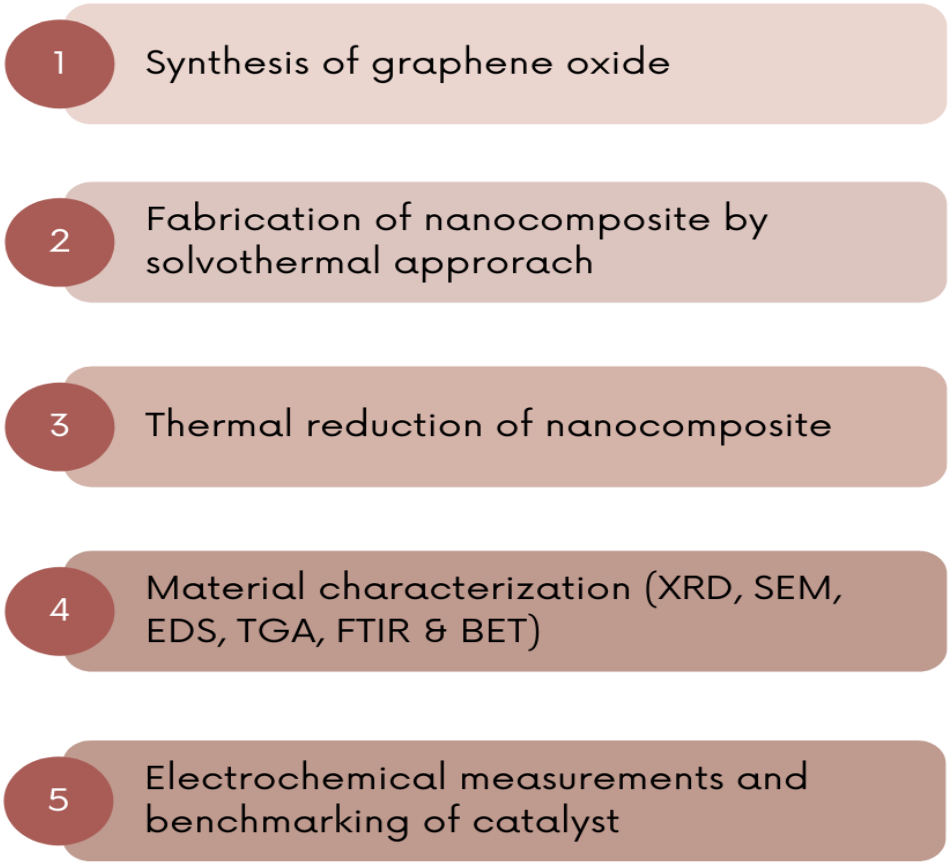


***Fig. 1.7*:** Thesis Breakdown

## 1.8 Reason/Justification for the Selection of the Topic

Early investigations into the development of lithium air cells focused mostly on common electrocatalyst materials derived from fuel cell applications, such as platinum, ruthenium, gold, iridium, and palladium, among others. As a result of the use of such catalyst materials, we learned a lot about the properties of electrode materials that might be used in these systems. In contrast, platinum-based electrodes were efficient in decreasing charge/discharge overpotentials, but no oxygen evolution was observed, confirming the absence of bifunctional characteristics in carbon-based materials. Research on the adjustment of novel material designs with significant mass transport characteristics

has been encouraged. Numerous materials have been synthesized and evaluated utilizing transition metal oxides and carbon as the substrate basis, but desired properties have not yet been achieved. It explores low weight, conductive, porous and bi-functionally active catalyst materials for these unique cell topologies. We decided to undertake thorough study in this field after seeing such a large gap between the importance of the situation and the lack of accessible remedies.

Metal organic frameworks are a new class of materials that exhibit interesting surface and morphological properties as a result of the coordination network chemistries that play a role in their formation. Metal organic frameworks are a type of material that has recently emerged and possesses interesting surface and morphological properties. Metal centers are surrounded by organic ligands that impart spatial distributions. MOFs have intrinsic hierarchical porosities, huge surface areas, an abundance of binding and active sites, and high ionic and electrical conductivities, making them ideal for energy storage. Because manganese oxide ($MnO_2$) was utilized in early versions of lithium air batteries, it suggests that manganese-based MOF materials should be explored for application in such systems. One specific framework, metal-based Nano Carbons, has been used for LIBs with good results. Based on the advantageous material properties, new Mn-N-C designs are anticipated to offer more important information regarding future energy materials for lithium air batteries.

## 1.9 Objectives of research

In this study, the goal is to manufacture a new Manganese-based Nano Carbon @reduced graphene oxide nanocomposite utilizing a solvothermal and thermal reduction method, describe the material characteristics, and conduct electrochemical measurements on the composite. Surface area and porosity measurements as well as elemental analysis are all possible methods of material characterization. Examples of such techniques include X-ray diffraction, Raman spectroscopy, Fourier transform infrared spectroscopy, and scanning electron microscope imaging. Cyclic voltammetry, linear sweep voltammetry, chronoamperometry, and electrochemical impedance spectroscopy would be used in

electrochemical measurements to determine catalytic activity for ORR, as well as methanol tolerance and stability.

## 1.10 Advantages & Areas of Application

This research offers in-depth insight into the future appearance of energy storage systems, as well as how material regulation will alter their internal composition and design in the future. Existing renewable energy power systems and automotive applications may benefit from the use of lithium-ion batteries. This scientific study yields compelling findings regarding the material characteristics, electrochemical performance, and stability of manganese MOF@rGO nanocomposite towards oxygen reduction and evolution reactions. This material, if used in lithium air batteries, has the potential to help these systems reach their full potential.

## Summary

This chapter provides an overview of the world's and Pakistan's energy requirements, as well as the country's current and future energy scenarios. As the country's energy demands are anticipated to grow in the future years, Pakistan has turned to a variety of renewable energy sources to meet its requirements. Electric energy storage (ESS) has the potential to make a significant contribution to reducing the imbalance between demand and supply during peak usage hours. There have been short discussions of a number of EES technologies in this area, with a particular focus on battery-based systems. A comparison of various battery technologies has been given, with lithium air batteries in particular being explored in more detail. The urgent need for electrocatalysts for ORR necessitates further research efforts to ensure their timely development.

## References


[1] A.B. Awan, Z.A. Khan, "Recent progress in renewable energy-Remedy of energy crisis in Pakistan," *Renew. Sust. Energ.*, vol. 33, pp. 236-253, 2014.

[2] D. Khan, "Impact of energy crisis on economic growth of Pakistan," *Int. J. Afr,* pp. 33-42, 2015.

[3] Z. Zhang, "A review of technologies and applications on versatile energy storage systems," *Renew. Sustain. Energy Rev.*, vol. 148, 2021.

[4] "U.S. Energy Information Administration. International energy statistics," http://www.eia.gov/cfapps/ipdbproject/IEDIndex3.cfm=tid=44&pid=44&aid=2..

[5] "The World Bank, Energy use.," http://data.worldbank.org/indicator/EG.USE. PCAP.KG.OE/countries/1W-PK-IN-CNNO- Redisplay=graph.

[6] A. D. Bank, "Proposed programmatic approach and policy-based loan for subprogram 1-Islamic Republic of Pakistan: Sustainable energy sector reform program," no. 47015-001, 2014.

[7] "National Transmission and Dispatch Company, Power system statistics," no. 39th edition, 2013-14.

[8] A Javaid, S. Hussain, A. Maqsood, Z. Arshad, A. Arshad, M. Idrees, *Int. J. Basic Appl. Sci,* 2011.

[9] S.R. Shakeel, J. Takala, W. Shakeel, "Renewable energy sources in power generation in Pakistan," *Renew. Sust. Energ,* vol. Rev. 64, pp. 421-434, 2016.

[10] M. Kamran, "Current status and future success of renewable energy in Pakistan," *Renew. Sust. Energ.,* vol. Rev. 82, pp. 609-617, 2018.

[11] N.A. Ahmed, M. Miyatake, A.K. Al-Othman, "Power fluctuations suppression of stand-alone hybrid generation combining solar photovoltaic/wind turbine and fuel cell systems," *Energ. Convers*, vol. Manage. 49, pp. 2711-2719, 2008.

[12] M. Whittingham, "Materials challenges facing electrical energy storage," *Mrs Bulletin*, pp. 411-419, 2008.

[13] P. Denholm, E. Ela, B. Kirby, M. Milligan, "Role of energy storage with renewable electricity generation," *United States, N. P.*, 2010.

[14] H.-F. Wang, Q. Xu, "Materials design for rechargeable metal-air batteries," *Matter*, pp. 565-595, 2019.

[15] J. Cho, S. Jeong, Y. Kim, "Commercial and research battery technologies for electrical energy storage applications," *Prog. Energ. Combust*, vol. 48, pp. 84-101, 2015.

# Chapter 2

# Literature review

## 2.1 Electrocatalyst materials for ORR

Recently, several energy materials have been synthesized and studied for oxygen reduction activity. Because hydrogen fuel cell technology relies on the concept of oxygen reduction on the cathode side of the membrane electrode assembly, it has traditionally used electrocatalyst materials. Advances in the development of electrocatalysts for fuel cells have prompted researchers to investigate the viability of existing materials for lithium air batteries. For fuel cell technology, noble metal catalysts are essential, and nano materials made from platinum, palladium, iridium, rubidium and manganese have been studied for their ability to perform two functions at the same time. These early studies not only gave information on the activity of the material, but also assisted in the establishment of a rigorous criteria for the needs of catalyst for lithium air applications. The ORR overpotentials were reduced using precious metal catalysts, but stability problems persisted. During the charging phase of Pt nanoparticles, parasitic breakdown of the electrolyte began to occur instead of oxygen evolution. Furthermore, noble metals cannot meet the quantity of material required to produce commercial batteries. Soon after, the emphasis of study in this field shifted to the exploration of plentiful earth metals with appropriate catalytic activity and functionalities that were comparable to or even superior to those of precious metals. In this manner, the cost of production and the performance of lithium-ion batteries may be standardized for commercial development [1].

After manufacturing oxygen electrocatalysis material, it's necessary to discuss about how measurements are acquired. ORR measurements are often performed in an acidic or alkaline electrolyte media. Depending on the needs of the experiment, 0.1M KOH solution is typically employed for alkaline medium. An electrochemical workstation with a rotating disc electrode assembly is used, to which a three-electrode electrochemical cell is attached. The electrochemical cell is made up of four main components: a reference

electrode, typically Ag/AgCl immersed in saturated KCl solution, a rotating disc working electrode, usually glassy carbon or platinum, a counter electrode, usually a Platinum wire, and electrolyte solution. Catalyst ink is made by distributing fine solid, Nafion ionic binder solution, and solvent. Drops of ink are dropped onto the surface of the working electrode and dried to form an impermeable coating on the active surface. As a result of this setup, cyclic voltammetry, linear sweep voltammetry, chronoamperometry, and energy impedance spectroscopy profiles are recorded, which are then used to calculate onset potential, half wave potential, maximum current density, overpotential, Tafel slope, and electrochemically active surface area, among other things. Oxygen molecules are adsorbed on the active sites and undergo reduction as a result of their interactions with water molecules and electrons during the process of ORR. The redox species produced during this reduction are highly reliant on the number of charge transfers during each stage of reduction. If four electrons are involved in this process, OH- is produced. OOH- is formed as a result of the transfer of two electrons. The oxygen evolution process occurs precisely in reverse and typically takes up for electrons [2, 3].

Now we will briefly describe several groups of chemicals that have recently been discovered to be efficient for oxygen electrocatalysis.

## 2.2 Single metal oxides

### 2.2.1 Cobalt oxides:

Cobalt oxides, a type of metal oxides, have been extensively utilized as electrocatalysts in recent study due to their outstanding performance in oxygen electrocatalysis. Cobalt oxides exhibit significant improvements and functions in their structures when coupled with carbon-based conductive materials, resulting in improved electrochemical characteristics. Different cobalt oxide architectures using novel synthesis routes have recently been reported, and the resulting catalysts have improved catalytic properties and conductivities, which can be attributed to the presence of $Co^{+2}$ oxidation state acting as active sites for ORR. He et al. showed that increasing the ratio of Co-MIL-101(Cr)-O resulted in a 1.16V overpotential rather than the 1.23V of pure MIL-101 (Cr) [4]. Due to

the complexity of the interactions occurring on the active sites, a complete understanding of the catalytic process is yet unknown, and the simple existence of oxidation states is inadequate to describe it. Different investigations have shown that transition metal oxides have an effect on catalytic activity, although their role in the process is not fully understood. To address this void, much research have been undertaken to unravel the role of transition metals and their structures on the atomic scale. Because synthetic methods have a large impact on catalyst quality, cobalt oxides with various morphologies such as spinal, reverse spinal, and amorphous have been investigated.

Maiyalagan et al. studied the catalytic activity of $LiCoO_2$, a common cathode material in lithium-ion batteries. The morphology of the $LiCoO_2$ phase is highly reliant on the synthesis circumstances and may take on various morphologies when exposed to varied temperature settings. They produced three samples of cobalt oxide with different compositions: lithiated spinel $LiCoO_2$, spinel $CoO_2$, and rock-salt like $LiCoO_2$, with spinel $LiCoO_2$ outperforming the others. This is due to the existence of numerous $Co^{+3}$ states that are readily oxidized when the OER potential is implemented. Out of all samples, this $Co^{+3}/Co^{+4}$ oxidation results in greater OER activity at lower applied potential. Although spinel $CoO_2$ has a similar structure to spinel, the distribution of Co ions has been changed, and Co ions are not easily oxidized to the $Co^{+4}$ state as they are in spinel. It demonstrates that, in addition to chemical composition, material structures play an important role in enabling electrochemical changes during ORR and OER. Spinel $LiCoO_2$ ORR activities were found to be weak, considerably lower than $CoO_2$. Lithium concentration was lowered, and a sample with a greater $Co^{+3}/Co^{+4}$ proportion and a lower degree of lithiation ($Li_{0.5}CoO_2$) was examined, which showed significantly improved ORR activity but suffered a slight reduction in alkaline medium stability. The structure, ORR, and OER activities of $CoO_2$, spinel $LiCoO_2$, and rock-salt like $LiCoO_2$, as well as a commercial $IrO_2$ catalyst, are shown in Fig. 2.1 [5].

Mesa et al. described a $MnO_x$ and $CoO_x$ supported N-doped carbon structure produced by pyrolysis and calcination. This matrix has the same cobalt oxide structure as $Co_3O_4$/NC, performs better than CoO, and has a 60 mV lower overpotential than a commercial Pt/C catalyst. This exceptional performance may be attributed to the presence of $CoN_x$ moieties in the matrix, which engage in the redox process [6].

A $Co_3O_4$/graphene composite with better catalytic capabilities than separate components has been produced. Nitrogen doping in $Co_3O_4$/graphene composites has shown minor material corrosion problems, a higher half-wave potential (0.83V), and lower ORR overpotentials than most previously reported catalysts [7].

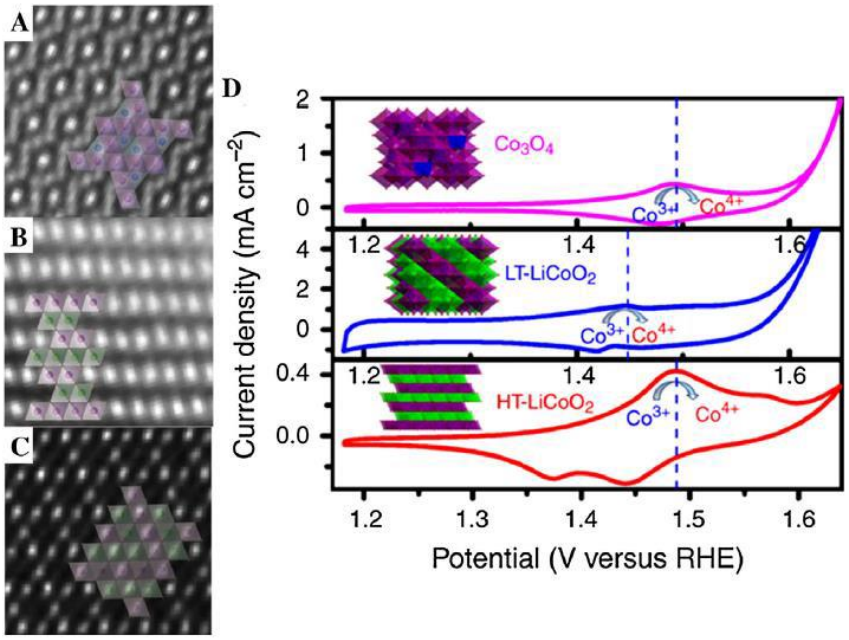


**Fig. 2.1:** High angle annular dark field scanning transmission electron microscope images of (A) $Co_3O_4$, (B) low temperature $LiCoO_2$ and (C) high temperature $LiCoO_2$. (D) Cyclic voltammograms of $Co_3O_4$ (purple), low temperature $LiCoO_2$ (blue) and high temperature $LiCoO_2$ (red) in 0.1M KOH [4]

### 2.2.2 Nickel Oxide:

However, despite the fact that nickel has greater conductivities than some of the transition metal catalysts, the use of nickel for ORR activity has been relatively underreported. Nickel possesses inherent characteristics such as high conductivity, stability, corrosion resistance, and strong ORR activity at low applied potential, making it a good choice for ORR applications, while other transition metal catalysts do not. Nickel's brucite structure includes $Ni^{+3}$ states, which have superior conductivities only second to noble metals, while $Ni^{+2}$ states have greater stabilities. $H_2$-$NiO_x$-MWCNT catalyst with long-term stability over 2000 minutes of operation and low onset potential has been developed recently using

nickel oxide with multiwalled carbon nanotubes and potassium borate solution (0.91V). There are several peaks in the ORR signal for this catalyst, indicating the participation of multiple oxidation states in oxidation, and an exceptional efficiency of 95% has been shown for ORR [8]. Nickel was investigated for catalytic activity because to its inherent ORR capabilities, however it was shown to have weak ORR activities. The reason for this is because dislocation of the Ni ion and subsequent reduction to $Ni^{+2}$ introduces an impurity phase into the catalyst, which is unfavorable to its quality. Liu et al. created a nickel nanoparticle dispersed graphene network with a large number of active sites [9]. However, despite the fact that graphene increased the conductivity of catalyst manifolds and produced superior ORR findings, the ORR activity remained unconvincing. These investigations lead us to the conclusion that, although nickel oxides perform well as catalytic materials, they may also be used to develop mixed metal oxide catalysts.

### 2.2.3 Iron Oxide:

Iron, like nickel, has not been applied to bifunctional applications, and its research in the field of catalysis has been done independently in ORR. Iron is thought to be rich in highly effective active sites such as cobalt for ORR catalysis, and it has a higher methanol tolerance than expensive Pt metal. While Pt-based catalysts are susceptible to methanol poisoning due to their catalytic capacity to oxidize methanol, iron is not. With its low cost and abundant availability, iron metal is a good candidate for electrocatalytic applications. However, stability concerns and a lack of bifunctional characteristics have limited its use, and scientists still have a long way to go to eliminate these concerns [10]. Iron oxide performs just moderately in ORR catalysis, according to a thorough research on reaction kinetics of transition metals [11]. Lyons and Brandon have done the majority of the research on iron oxide-based ORR catalysts, using passivated electrode layers for testing. They suggested that iron may be readily oxidized in a variety of settings, resulting in catalysis developing passive layers on the exposed region, resulting in generations experiencing inconsistency each time a new material is introduced. During the development of the oxide layer, $Fe^{+2}$ is transformed to $Fe^{+3}$, while $Fe^{+6}$ sites are thought to be responsible for electrocatalytic activity. Furthermore, the values of Tafel slopes change when the voltage window is reversed. Because of this instability and

unpredictability, iron oxides are less suitable for OER, and developing a bifunctional electrocatalyst seems challenging [12].

### 2.2.4 Manganese Oxide:

Manganese is one of the most ubiquitous elements on the planet and is readily accessible as a chemical compound. The inspiration for using manganese for electrocatalytic purposes came from its presence in natural photosynthetic processes, where it exists in metal organic complex form and facilitates water splitting. Mn exists in thirty distinct structures and three polyvalent forms due to its octahedral crystal structure. This octahedral structure provides for a variety of shapes and forms that may be adjusted for electrocatalytic reasons. Layered and tunnel structures are two of the most frequent shapes that have shown remarkable catalytic capabilities. It is worthwhile to note out which structures, among the many that are accessible, perform better for bifunctional oxygen electrocatalytic activities and why this is the case. Gorlin et al. created $Mn_2O_3$ nanofilms and studied their catalytic properties. $Mn_2O_3$ with $Mn^{+3}$ oxidation state demonstrated excellent ORR activity, outperforming iridium and ruthenium-based catalysts and being on par with platinum. As indicated in Fig. 2.2, the half-wave potential of OER (1.77 V) was discovered near to the Iridium catalyst [13].

Meng et al. produced four morphological forms of manganese oxide: alpha, beta, gamma, and amorphous oxides. Alpha and beta structures resembled tunnels, while gamma and amorphous structures resembled sheet-like layered structures. Alpha manganese oxide beat the other three oxides in terms of reduced ORR overpotentials, catalytic stability, and reaction kinetics for ORR. Alpha manganese oxide demonstrated a 780 mV overpotential, a 20-mV voltage decrease after 10,000s of operation. Similarly, in OER tests, it beat all other catalysts in terms of greater current density and lower overpotential values. This performance may be attributed to the high penetration of $Mn^{+3}$ states as well as significant quantities of $K^+$ concentration, both of which are believed to have a favorable effect on attaining greater activity. Alpha manganese oxide has the most surface area, pore volume, surface defects, and accessible active centers, indicating that it has a higher proclivity to

adsorb oxygen molecules and oxidize water. Furthermore, it was the only candidate that showed evidence of the four electron transport mechanisms listed below [14].

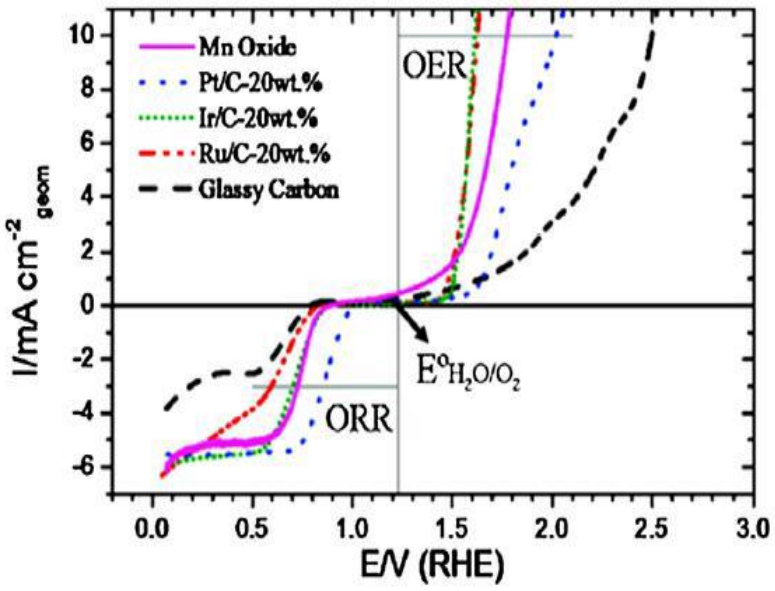


**Fig. 2. 2:** ORR and OER activity from Linear sweep voltammogram of Mn oxide, Pt/C, Ir/C, Ru/C and bare glassy carbon electrode [13]

As, α-$MnO_2$ has shown catalytic capability, it is reasonable to construct various nanostructures using carbon materials. In a recent research, three carbon structured versions of α - $MnO_2$ were produced using nanotube, nanowire, and nanoparticle topologies. Because to the uniform distribution of oxygen and hydroxyl ions, as well as the chemisorption of water molecules, nanowire demonstrated superior ORR activity [15]. Another research implanted porphyrin and phthalocyanines in nitrogen doped amorphous carbon as transition metal precursors. Metal oxide and metal nitride moieties were generated during calcination. Metal oxide was enclosed by a ringed Mn-$N_x$ structure, yielding significant effects [16].

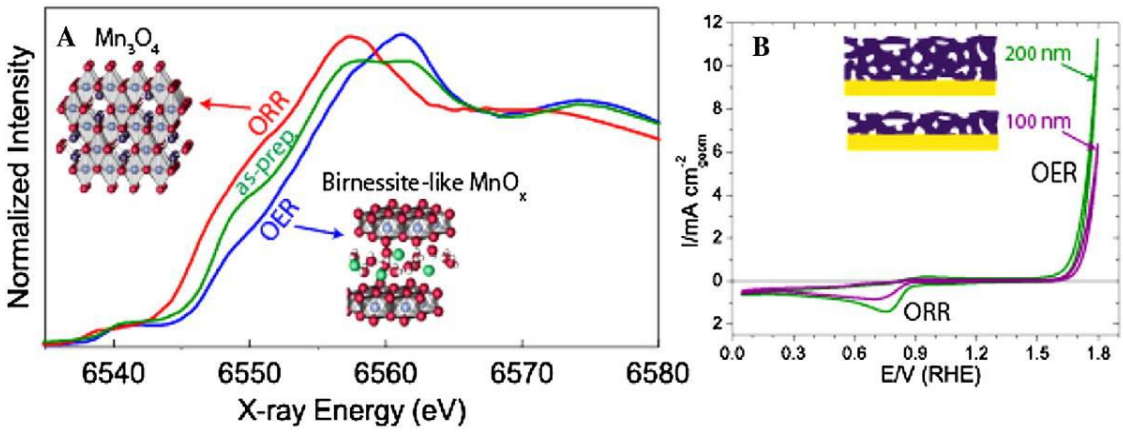


**Fig. 2. 3:** High resolution transmission electron microscope images of (A) solvent free α-$MnO_2$-SF, (B) amorphous manganese oxide, (C) ß-$MnO_2$ and (D) OER electroactivity of α-$MnO_2$-SF, AMO, ß-$MnO_2$ and δ-$MnO_2$

X-ray absorption spectroscopy of a simple $MnO_x$ impregnated on gold coated silicon nitride, $MnO_x$/Ag-$Si_3N_4$, showed the presence of MnO and $MnO_2$ structures. On glassy carbon, $MnO_x$/Ag-$Si_3N_4$ occupied Birnessite-like manganese oxide structure. When ORR potentials were applied, $MnO_x$ transitioned to higher oxidation states, conferring electrocatalytic activity to the Birnessite-like structure, while the α-$Mn_3O_4$-like structure did not exhibit this behavior [17]. Scientists have also described a α-$MnO_2$ composite with a MIL-101(Cr) metal organic framework [18]. Gao et al. utilized PVC as a carbon source in conjunction with Sulphur doped manganese oxide as part of a cost-cutting approach to decrease the cost of the source material. This combination demonstrated higher onset potentials for ORR [19]. Doping carbon materials with N, S, and P may assist to improve catalytic capabilities by reordering electronic distributions [20, 21]. Gao et al. used inert environment pyrolysis to create a high graphitized MnO/S-GC catalyst. To circumvent the expensive cost of graphene, a stainless steel and MnO composite was utilized, where porous MnO catalyzes ORR and provides diffusion channels to stainless steel for catalysis [22].

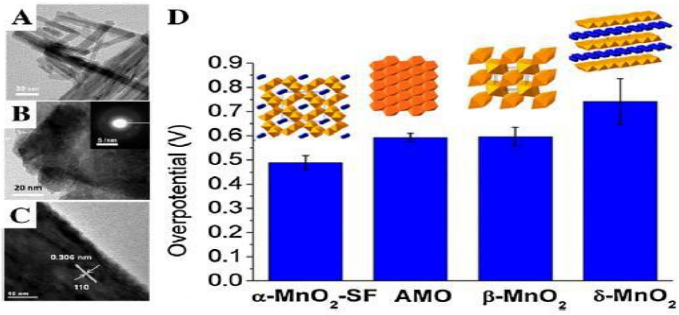


**Fig. 2. 4:** (A) X-ray absorption near edge spectroscopy of as prepared $MnO_x$/Au-$Si_3N_4$ film and on applied conditions of catalytic activity. (B) Cyclic voltammetry with 100 nm and 200 nm thickness of $MnO_x$ catalyst [17]

## 2.3 Mixed transition metal oxides:

Combining two or three different transition metal oxides with distinct catalytic characteristics may be a helpful strategy for creating electrocatalysts, allowing researchers to make the most of the potential of transition metal oxides. In common synthesis technique, one metal oxide is ingrained within the lattice of another, resulting in homogeneous chemistry and changed lattice characteristics that are adjustable for the desired use. Binary transition metal oxides are more often reported for oxygen electrocatalysis, with a few instances of ternary oxides exhibiting remarkable catalytic activity. In this section, we will look into binary and ternary oxides for catalytic activity [23]. As both cobalt and manganese have established functions and are viable for ORR, a combination of nanotubes such as -$MnO_2$ and cubic $Co_3O_4$ has been produced using prolonged solvothermal methods. The hybrid catalyst's onset potential was found to be in the middle of that of an individual catalyst, but the current density increased by a factor of two to three times [24]. Graphene-embedded cobalt manganese oxide of the spinel type has been described, with conductivity significantly enhanced as a result of strong bonding between the conductive and oxide phases [25]. When coupled with binary oxide, nitrogen doping of graphene may offer extra catalytic sites. This method has been validated by the successful fabrication of $CoMn_2O_4$/NG, as well as good results for Zn-air batteries.

The increasing usage of carbon materials as conductive supports has several drawbacks, including the deterioration of catalyst stability. However, certain materials, such as carbon nanotubes, are impervious to it. When combined with binary oxides, N-inherent doping's

structural strength and stiffness may offer a synergistic impact. Using CNTs with internal round bases, one study created Co-Mn spinel structures. Four such structures were produced and thermally treated to split tubes, revealing active spinel Co-Mn structures for catalysis. Heat treatment not only enhanced surface area but also created new locations for redox reaction anchoring and facilitation. During the ORR, the resulting catalyst provided higher onset potentials as well as a high current density. Co-Mn salt grown over CNTs to generate $Co_xMn_{1-x}O$@CNTs nanoparticles has shown that CNTs without doping may also act as an effective catalyst.

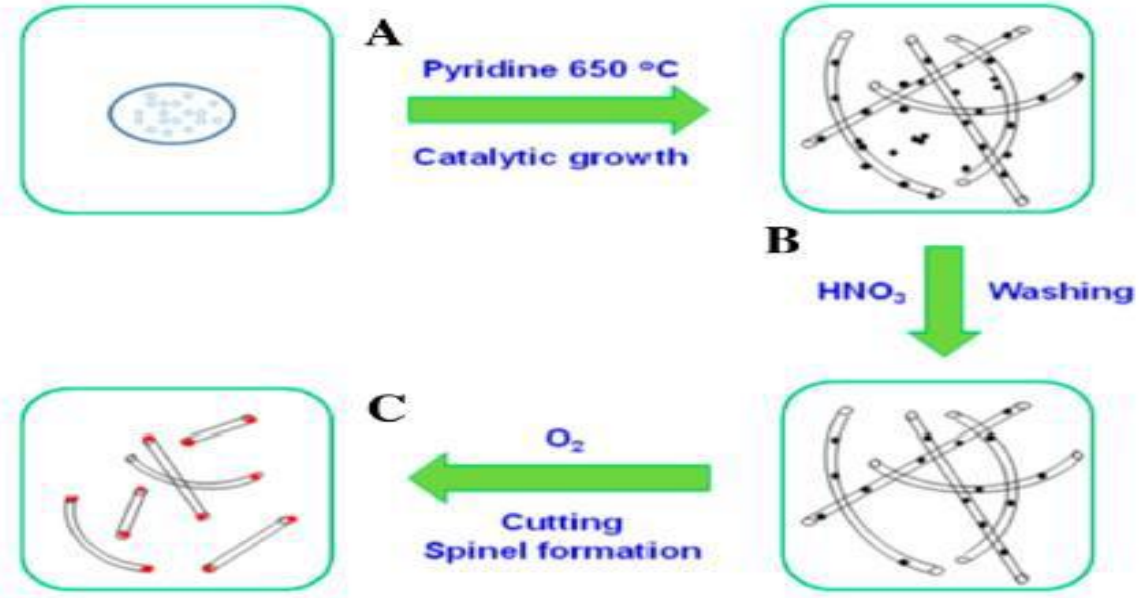


**Fig. 2. 5:** Synthesis layout of spinel Mn-Co oxide NPs in NCNTs [26]

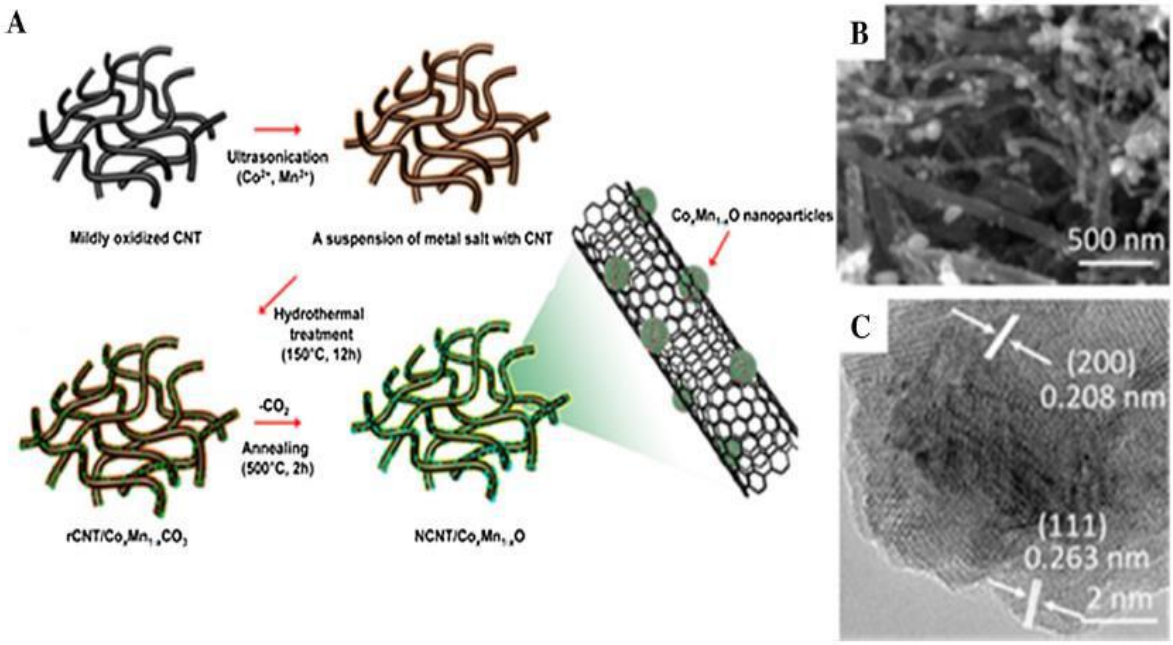


**Fig. 2. 6:** Schematic diagram of preparation of $Co_xMn_{1-x}O$ @NCNTs along with TEM images [27]

In order to enhance material conductivity and ORR activity, nickel has been mixed with manganese oxide, which is not a good ORR catalyst but boosts the conductivity of the structure, providing large current peaks for OER. Three distinct morphologies of -$MnO_2$ structures were produced using solvent free and reflux techniques, including nanowire, nanorod, and dendritic forms. A variety of particle sizes were used in the production of the catalysts, which included tunneling features. The structural addition of $Ni^{+2}$ decreased the $Mn^{+3}/Mn^{+4}$ proportion and provided significant current and reduction densities [28]. As a consequence of the changed pore diameters and surface areas caused by $Ni^{+2}$, as well as the increased oxygen vacancies, the performance of the system was improved but $H_2O_2$ degradation was increased. Among them, solvent-free nanorods demonstrated superior activity [28]. Similar to this, a mixed oxide of $NiCo_2O_4$ has also been produced, which illustrates how the quantity of metal loading may influence the catalytic activity of a lithium-air battery. As the quantity of catalyst in the slurry for electrode deposition rises, it enhances activity up to a point of 20%, beyond which specific capacity begins to decline [29].

Through the use of binary oxides, researchers have gained a greater knowledge of how various oxides may interact with one another to enhance electroactivity characteristics and material designs, resulting in improved performance. This method has been expanded by mixing more than two metals to provide changed crystal structures and physical characteristics such as pore size, surface area, morphology, and active site production. Metals are taken up in precursors or doped during intermediary stages to produce this effect. Ternary oxides are often composed of precious metals or non-transition metals, which may be used to improve the functions and accessory characteristics of the material. These include copper cobalt oxide embedded in niobium doped Titania ($CuCoO_2$/Ni-$TiO_2$) [30], $MnO_2$@$LaCoO_3$ and $MnO_2$@$Nd_2IrO_7$ [31], iron cobalt and nickel oxide (Fe-Co-Ni-O) [32], cobalt and nickel with $TeO_2$ Co, Ni-$TeO_2$ [33]. Other kinds of materials have also been synthesized for this purpose. We can only reveal so much for the sake of brevity.

The following table contains information about electrochemical parameters.

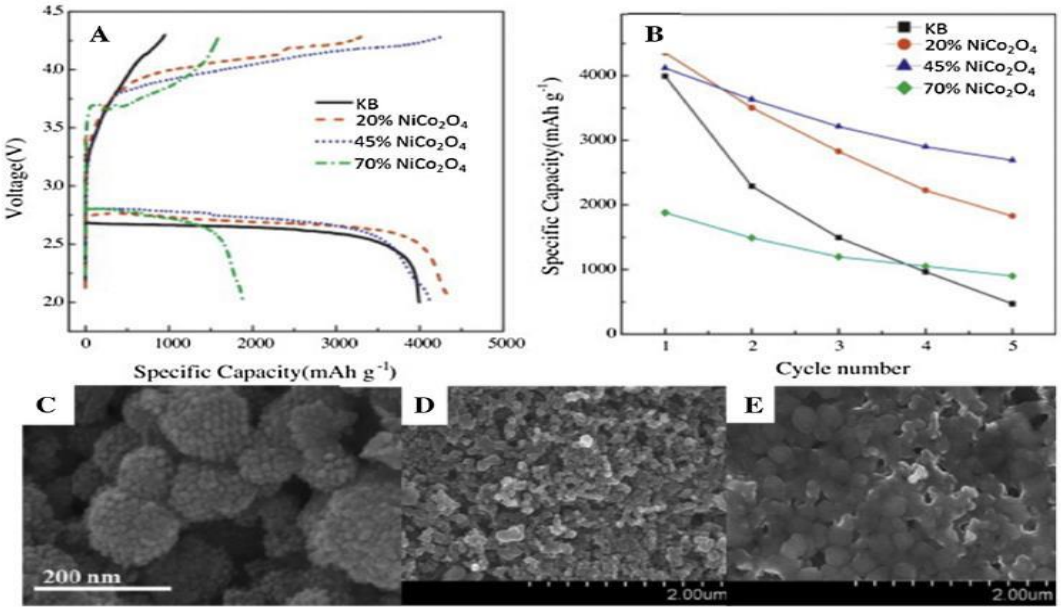


**Fig. 2. 7:** (A)Discharge/ charge curves and (B) cyclic performance test of $NiCo_2O_4$ for Li-$O_2$ batteries [28] and (C-E) SEM images of $NiCo_2O_4$

Table 2. 1: Performance parameters of some recently reported electrocatalysts for ORR

| Sr #. | Catalyst ID | Oxygen reduction reaction | | | | |
|---|---|---|---|---|---|---|
| | | **$E_{onset}$** V vs RHE | **$E_{1/2}$** V vs RHE | **n** | **Tafel slope** $mVdec^{-1}$ | **Electrolyte** |
| 1. | Fe/N/C@BMZIF [34] | 0.99 | 0.85 | 3.9 | - | 0.1M KOH |
| 2. | $Co_3O_4$–C Nanowire Arrays [35] | 0.9 | 0.83 | 3.7 | 62.3 | 1M KOH |
| 3. | Co-N-CNTs [36] | 0.97 | 0.90 | 4 | - | 0.1M KOH |
| 4. | C-MOF-C2-900 [37] | - | 0.82 | 3.8 | 79 | 0.1M KOH |
| 5. | NC-Co3O4-90 [38] | 0.97 | 0.9 | 3.9 | - | 1M KOH |
| 6. | Co–Nx/C Nanorod array [39] | - | 0.87 | 3.9 | 62.3 | 1M KOH |
| 7. | Fe0.5Co0.5Ox/N-rGO [40] | - | - | 3.9 | 30.1 | 0.1 M KOH 1 M KOH |
| 8. | NiFe-LDH/Co, N-Carbon Nanoframe [41] | 0.89 | 0.79 | 3.9 | 60 | 0.1 M KOH |
| 9. | Fe@CNG/ NCNTs [42] | 0.93 | 0.84 | 4 | 163 | 0.1 M KOH 1 M KOH |
| 10. | Fe/Fe3C@ 3D NGraphene [43] | 0.93 | 0.77 | 3.9 | - | 0.1 M KOH |
| 11. | NCNTFs [44] | 0.97 | 0.87 | 3.9 | 93 | 0.1 M KOH |
| 12. | Co/CoxSy@SNCF-800 [45] | 0.83 | 0.74 | 3.9 | 68 | 0.1 M KOH |
| 13. | NiFe@NCX [46] | 1.03 | 0.86 | 3.9 | 60.1 | 0.1 M KOH |

## Summary

A literature overview of several transition metal oxides in single, binary, and ternary oxide forms is given in this chapter. Cobalt, nickel, iron, and manganese oxides in polymorphic forms, as well as composites with various carbon structures or doped metals, have been studied and tabulated.

## References


[1] S. Yang, P. He, H. Zhou, "Research progresses on materials and electrode design towards key challenges of Li-air batteries," *Energy Storage Mater,* vol. 13, pp. 29-48, 2018.

[2] Y. Jiao, Y. Zheng, M. Jaroniec, S.Z. Qiao, "Design of electrocatalysts for oxygen- and hydrogen-involving energy conversion reactions," *Chem. Soc,* no. 44, pp. 2060-2086, 2015.

[3] B. Zhu, D. Xia, R. Zou, "Metal-organic frameworks and their derivatives as bifunctional electrocatalysts," *Coord. Chem.,* no. 376, pp. 430-448, 2018.

[4] X. He, F. Yin, G. Li, "Co/metal–organic-framework bifunctional electrocatalyst: the effect of the surface cobalt oxidation state on oxygen evolution/reduction reactions in an alkaline electrolyte," *Int. J. Hydrog. Energy,* no. 40, pp. 9713-9722, 2015.

[5] T. Maiyalagan, K.A. Jarvis, S. Therese, P.J. Ferreira, A. Manthiram, "A. Manthiram, Spinel-type lithium cobalt oxide as a bifunctional electrocatalyst for the oxygen evolution and oxygen reduction reactions," *Nat. Commun.,* no. 5, pp. 1-8, 2014.

[6] J. Masa, W. Xia, I. Sinev, A. Zhao, Z. Sun, S. Grützke, P. Weide, M. Muhler, W. Schuhmann, "$Mn_xO_y$/NC and $Co_xO_y$/NC nanoparticles embedded in a nitrogen-doped carbon matrix for high-performance bifunctional oxygen electrodes," *Angew. Chem,* no. 53, pp. 8508-8512, 2014.

[7] Y. Liang, Y. Li, H, Wang, J. Zhou, J. Wang, T. Regier, H. Dai, "Co3O4 nanocrystals on graphene as a synergistic catalyst for oxygen reduction reaction," *Nat. Mater,* no. 10, p. 780, 2011) .

[8] X. Yu, T. Hua, X. Liu, Z. Yan, P. Xu, P. Du, "Nickel-based thin film on multiwalled carbon nanotubes as an efficient bifunctional electrocatalyst for water splitting," *ACS Appl. Mater. Inter,* no. 6, pp. 15395-15402, 2014.

[9] X. Liu, W. Liu, M. Ko, M. Park, M.G. Kim, P. Oh, S. Chae, S. Park, A. Casimir, G. Wu, J. Cho, "Metal (Ni, Co)-metal oxides/graphene nanocomposites as multifunctional electrocatalysts," *Adv. Funct. Mater.,* no. 25, pp. 5799-5808, 2015.

[10] X. Wang, M. Waje, Y. Yan, "Methanol resistant cathodic catalyst for direct methanol fuel cells," *J. Electrochem. Soc.,* no. 151, p. 2183, 2004.

[11] R. Scarr, "The mechanism of oxygen evolution on nickel, platinum, and other metals," *J. Electrochem. Soc.,* no. 116, p. 1526, 1969.

[12] M.E.G. Lyons, M.P. Brandon, "Oxygen evolution reaction on passive oxide covered transition metal electrodes in aqueous alkaline solution," *Int. J. Electrochem,* no. 3 , pp. 1386-1424, 2008.

[13] Y. Gorlin, T.F. Jaramillo, "A bifunctional nonprecious metal catalyst for oxygen reduction and water oxidation," *J. Am. Chem. Soc.,* no. 132, pp. 13612-13614, 2010.

[14] Y. Meng, W. Song, H. Huang, Z. Ren, S.-Y. Chen, S.L. Suib, "Structure–property relationship of bifunctional MnO2 nanostructures: highly efficient, ultra-stable electrochemical water oxidation and oxygen reduction reaction catalysts identified in alkaline media," *J. Am. hem. Soc.,* no. 136, pp. 11452-11464, 2014.

[15] K. Selvakumar, S.M.S. Kumar, R. Thangamuthu, G. Kruthika, P. Murugan, "Development of shape-engineered α-MnO2 materials as bi-functional catalysts for oxygen evolution reaction and oxygen reduction reaction in alkaline medium," *Int. J. Hydrog. Energy,* no. 39, pp. 21024-21036, 2014.

[16] J. Masa, W. Xia, I. Sinev, A. Zhao, Z. Sun, S. Grützke, P. Weide, M. Muhler, W. Schuhmann, "$Mn_xO_y$/NC and $Co_xO_y$/NC nanoparticles embedded in a nitrogen-doped carbon matrix for high-performance bifunctional oxygen electrodes," *Angew. Chem.,* no. 53, pp. 8508-8512, 2014.

[17] Y. Gorlin, B. Lassalle-Kaiser, J.D. Benck, S. Gul, S.M. Webb, V.K. Yachandra, J. Yano, T.F. Jaramillo, "In situ X-ray absorption spectroscopy investigation of a bifunctional manganese oxide catalyst with high activity for electrochemical water oxidation and oxygen reduction," *J. Am. Chem. Soc.,* no. 135, pp. 8525-8534, 2013.

[18] F. Yin, G. Li, H. Wang, "Hydrothermal synthesis of α-$MnO_2$/MIL-101 (Cr) composite and its bifunctional electrocatalytic activity for oxygen reduction/evolution reactions," *Catal. Commun.,* no. 54, pp. 17-21, 2014.

[19] Y. Gao, H. Zhao, D. Chen, C. Chen, F. Ciucci, "In situ synthesis of mesoporous manganese oxide/sulfur-doped graphitized carbon as a bifunctional catalyst for oxygen evolution/reduction reactions," *Carbon,* no. 94, pp. 1028-1036, 2015.

[20] S. Wang, L. Zhang, Z. Xia, A. Roy, D.W. Chang, J.-B. Baek, L. Dai, "BCN graphene as efficient metal-free electrocatalyst for the oxygen reduction reaction," *Angew. Chem.,* no. 51, pp. 4209-4212, 2012.

[21] K. Qu, Y. Zheng, S. Dai, S.Z. Qiao, "Graphene oxide-polydopamine derived N, S co doped carbon nanosheets as superior bifunctional electrocatalysts for oxygen reduction and evolution," *Nano Energy,* no. 19, pp. 373-381, 2016.

[22] J.W.D. Ng, M. Tang, T.F. Jaramillo, "A carbon-free, precious-metal-free, high performance O2 electrode for regenerative fuel cells and metal–air batteries," *Energ. Environ. Sci.*, no. 7, pp. 2017-2024, 2014.

[23] C. Yuan, H.B. Wu, Y. Xie, X.W. Lou, "Mixed transition-metal oxides: design, synthesis, and energy-related applications," *Angew. Chem,* no. 53, pp. 1488-1504, 2014.

[24] G. Du, X. Liu, Y. Zong, T.S.A. Hor, A. Yuc, Z. Liu, "Co3O4 nanoparticle-modified MnO2 nanotube bifunctional oxygen cathode catalysts for rechargeable zinc-air batteries," *Nanoscale*, no. 5, pp. 4657-4661, 2013.

[25] L. Wang, X. Zhao, Y. Lu, M. Xu, D. Zhang, R.S. Ruoff, K.J. Stevenson, J.B. Goodenough, "$CoMn_2O_4$ spinel nanoparticles grown on graphene as bifunctional catalyst for lithium-air batteries," *J. Electrochem. Soc.*, no. 158, p. 1379, 2011.

[26] M. Prabu, P. Ramakrishnan, S. Shanmugam, "CoMn2O4 nanoparticles anchored on nitrogen-doped graphene nanosheets as bifunctional electrocatalyst for rechargeable zinc air battery," *Electrochem. Commun.*, no. 41, pp. 59-63, 2014.

[27] X. Liu, M. Park, M.G. Kim, S. Gupta, X. Wang, G. Wu, J. Cho, "High-performance non-spinel cobalt–manganese mixed oxide-based bifunctional electrocatalysts for rechargeable zinc-air batteries," *Nano Energy*, no. 20, pp. 315-325, 2016.

[28] E.M. Benbow, S.P. Kelly, L. Zhao, J.W. Reutenauer, S.L. Suib, "Oxygen reduction properties of bifunctional α-manganese oxide electrocatalysts in aqueous and organic electrolytes," *J. Phys. Chem.*, no. 115, pp. 22009-22017, 2011.

[29] D. Zhao, J.-L. Shui, L.R. Grabstanowicz, C. Chen, S.M. Commet, T. Xu, J. Lu, D.-J. Liu, "Highly efficient non-precious metal electrocatalysts prepared from one-pot synthesized zeolitic imidazolate frameworks," *Adv. Mater.*, no. 26, pp. 1093-1097, 2014.

[30] M.D Koninck, P. Manseau, B. Marsan, "Preparation and characterization of Nb-doped TiO2 nanoparticles used as a conductive support for bifunctional $CuCo_2O_4$ electrocatalyst," *J. Electroanal. Chem.*, no. 611, pp. 67-79, 2007.

[31] P. Hosseini-Benhangi, M.A. Garcia-Contreras, A. Alfantazi, E.L. Gyenge, "Method for enhancing the bifunctional activity and durability of oxygen electrodes with mixed oxide electrocatalysts: Potential driven intercalation of potassium," *J. Electrochem. Soc.*, no. 162, p. 1356, 2015 .

[32] R.D.L. Smith, M.S. Prévot, R.D. Fagan, Z. Zhang, P.A. Sedach, M.K.J. Siu, S. Trudel, "Photochemical route for accessing amorphous metal oxide materials for water oxidation catalysis, Science," *Science* , no. 340, pp. 60-63, 2013.

[33] V. Rashkova, S. Kitova, I. Konstantinov, T. Vitanov, "Vacuum evaporated thin films of mixed cobalt and nickel oxides as electrocatalyst for oxygen evolution and reduction," *Electrochim. Acta.,* no. 47, pp. 1555-1560, 2002.

[34] M. Wang, T. Qian, J. Zhou, C. Yan, "An efficient bifunctional electrocatalyst for a zinc–air battery derived from Fe/N/C and bimetallic metal-organic framework composites," *ACS Appl. Mater. Inter.,* no. 9, pp. 5213-5221, 2017.

[35] J.-T. Ren, G.-G. Yuan, C.-C. Weng, Z.-Y. Yuan, "Rationally designed $Co_3O_4$–C nanowire arrays on Ni foam derived from metal organic framework as reversible oxygen evolution electrodes with enhanced performance for Zn-air batteries," *ACS Sustain. Chem. Eng.,* no. 6, pp. 707-718, 2018.

[36] T. Wang, Z. Kou, S. Mu, J. Liu, D. He, I.S. Amiinu, W. Meng, K. Zhou, Z. Luo, S. Chaemchuen, F. Verpoort, "2D dual-metal zeolitic-imidazolate-framework-(ZIF)-derived bifunctional air electrodes with ultrahigh electrochemical properties for rechargeable zinc-air batteries," *Adv. Funct. Mater.,* no. 28, 2018.

[37] M. Zhang, Q. Dai, H. Zheng, M. Chen, L. Dai, "Novel MOF-derived Co@ N-C bifunctional catalysts for highly efficient Zn-air batteries and water splitting," *Adv. Mater.,* no. 30, 2018.

[38] C. Guan, A. Sumboja, H. Wu, W. Ren, X. Liu, H. Zhang, Z. Liu, C. Cheng, S.J. Pennycook, J. Wang, "Hollow Co3O4 nanosphere embedded in carbon arrays for stable and flexible solid-state zinc-air batteries," *Adv. Mater,* no. 29, 2017.

[39] I.S. Amiinu, X. Liu, Z. Pu, W. Li, Q. Li, J. Zhang, H. Tang, H. Zhang, S. Mu, "From 3D ZIF nanocrystals to Co-Nx/C nanorod array electrocatalysts for ORR, OER, and Znair batteries," *Adv. Funct. Mater.,* no. 28, 2018.

[40] L. Wei, H.E. Karahan, S. Zhai, H. Liu, X. Chen, Z. Zhou, Y. Lei, Z. Liu, Y. Chen, "Amorphous bimetallic oxide-graphene hybrids as bifunctional oxygen electrocatalysts for rechargeable Zn-air batteries," *Adv. Mater.,* no. 29, 2017.

[41] Q. Wang, L. Shang, R. Shi, X. Zhang, Y. Zhao, G.I.N. Waterhouse, L.-Z. Wu, C.-H. Tung, T. Zhang, "NiFe layered double hydroxide nanoparticles on Co, N-codoped carbon nanoframes as efficient bifunctional catalysts for rechargeable zinc-air batteries," *Adv. Energy Mater.,* no. 7, 2017.

[42] Q. Wang, Y. Lei, Z. Chen, N. Wu, Y. Wang, B. Wang, Y. Wang, "Fe/$Fe_3C$@ C nanoparticles encapsulated in N-doped graphene-CNTs framework as an efficient bifunctional oxygen electrocatalyst for robust rechargeable Zn-air batteries," *J. Mater. Chem.,* no. 6, pp. 516-526, 2018.

[43] Y. Lai, W. Chen, Z. Zhang, Y. Qu, Y. Gan, J. Li, "Fe/$Fe_3C$ decorated 3-D porous nitrogen-doped graphene as a cathode material for rechargeable Li–$O_2$ batteries," *Electrochim. Acta*, no. 191, pp. 733-742, 2016.

[44] B.Y. Xia, Y. Yan, N. Li, H.B. Wu, X.W. Lou, X. Wang, "A metal-organic framework derived bifunctional oxygen electrocatalyst," *Nat. Energy*, 2016.

[45] S. Liu, X. Zhang, G. Wang, Y. Zhang, H. Zhang, "High-Efficiency Co/CoxSy@S,Ncodoped porous carbon electrocatalysts fabricated from controllably grown sulfur and nitrogen-including cobalt-based MOFs for rechargeable zinc–air batteries," *ACS Appl. Mater. Inter.*, no. 9, p. 34269–34278, 2017.

[46] J. Zhu, M. Xiao, Y. Zhang, Z. Jin, Z. Peng, C. Liu, S. Chen, J. Ge, W. Xing, "Metalorganic framework-induced synthesis of ultrasmall encased NiFe nanoparticles coupling with graphene as an efficient oxygen electrode for a rechargeable Zn-air battery," *ACS Catalysis,*, no. 6, pp. 6335-6342, 2016.

# CHAPTER 3

# Experimentation and Characterization Methods

In recent years, scientists have been more interested in metal organic frameworks due to their distinctive structures, compositions, and functions. Metal organic frameworks, or MOFs, are produced by following coordination chemistry principles in which short or long chains of organic linker encircle and connect metal centers or clusters. MOFs are composed of heavy transition metals such as Co, Mn, Zn, Zr, Fe, Cu, etc., as opposed to other coordination polymers such as covalent organic frameworks (COF), where lighter elements serve as coordinating In a MOF structure, ligands create various sized chains with metal clusters, which subsequently form cross-linkages in one, two, or three dimensions, resulting in a variety of spatial arrangements. MOFs have very porous structures with readily accessible binding sites, which may be advantageous for gas absorption, purification, catalysis, and sensing applications. We'll focus on typical MOF synthesis techniques here. MOF are most often produced using traditional techniques such as solvothermal, mechanochemical, electrochemical, microwave, and Sonochemical synthesis. Typically, solution phase synthesis is used in the majority of methods for crystallization of MOF from precursor solution mixtures. Porous structures are clogged by a high number of contaminants and inclusions, some of which are covalently linked to one another. Purification and activation procedures are required before application to produce phase pure and light structures. Typically, volatile solvents that may dissolve contaminants and clear pores are employed for purification. Material activation is done in an inert gas atmosphere at a high temperature to eliminate weakly and firmly bound solvent molecules and alien entities. Post-synthesis modifications like as ligand exchange, metal exchange, and stratified synthesis may further tune functional groups. All of these processes may substantially increase pore volumes, active surface areas, and structures of materials, all of which have a direct effect on their electrocatalytic activity [1].

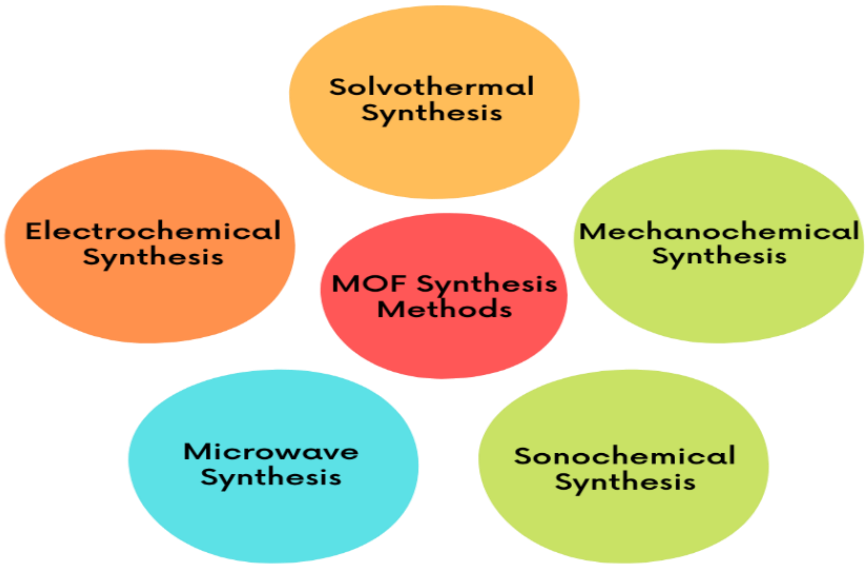


***Fig. 3. 1:*** Classification of different synthesis techniques for MOF preparation

## 3.1 Synthesis method

### 3.1.1 Solvothermal Route

Solvothermal synthesis has long been thought to be the most common method for producing MOFs. It may be classified into various groups depending on the kind of solvent employed, for example, when water is used as the solvent, the technique is referred to as hydrothermal. It is really a specific method in a controlled environment, just as the name solvothermal would seem. The term "non-solvothermal" refers to a simple solution mixing reaction that is carried out in standard class ware with the help of mild heating and vigorous stirring at atmospheric pressures. It is preferable to use a non-solvothermal approach for those chemicals that arise spontaneously and are thermodynamically advantageous in the forward direction. For transforming precursor into product, the solvothermal method requires high temperatures and in situ pressure buildup. It is carried out in a sealed atmosphere with reactor interior materials that are chemically inert and thermally stable. In the vapour phase, homogeneous diffusion and reagent collisions may occur when heating conditions are near or above the boiling point of the solvent. Extremely high pressures are maintained within a closed vessel via the use of solvent evaporation or external pumps. Solvothermal technique needs metal salt, organic

connectivity, miscible solvents and pH stabilizer in certain instances. Salt concentration, temperature, and pH changes are adjusted for maximum reaction yield [2].

Many useful MOF structures have been developed using a non-solvothermal method. Successful syntheses of ZIF-8, ZIF-67, MOF-5, MOF-74, and MOF-177 have been reported [3, 4, 5]. A few changes have also been made to non-solvothermal techniques, such as establishing a concentration gradient by cooling, layering the solvent with an intermediary medium, and slow diffusion. Huang et al. discovered that ZIF-8 is produced by mixing zinc salt with ammonia in a ZIF precursor solution [6]. The solvothermal method, on the other hand, provides significant procedural benefits by allowing for more control over working conditions and less disruptions from nearby entities due to the closed reaction set-up. Highly crystalline and homogeneous products may be produced since the reaction happens at higher pressures built up in situ. Probabilities like as reproducibility, crystallinity and scale-up are essential to any MOF synthesis technique's dependability and validity; however, the solvothermal approach dispenses with these to a large. Another essential element is the procedure's duration, which may allow for gradual crystallization and homogenous product, which can be achieved with this technique. Due to the fact that the solvothermal technique is performed in a specific container/vessel (e.g., a Teflon-lined stainless-steel autoclave), the time may range from hours to days or even months. Recent reports focusing on the impact of synthesis method on the structural characteristics of MOF-5 asserted that solvothermal synthesis increased the material's surface area by an astonishing 68% [7, 8]. Thermal stability was obtained above 500°C when this method was replicated for Zr-MOF UiO-66 [9]. Changing reaction conditions may also influence structural differences and morphologies.


**Fig 3.2:** Autoclave used for the hydrothermal synthesis technique.

## 3.2 Characterization Techniques

### 3.2.1 Powder X-ray Diffraction:

X-ray powder diffraction is a non-destructive analytical method used to assess crystal structure, identify crystalline phases, and determine purity. Aside from that, it aids in revealing information on crystal structure type, average crystallite size, crystal flaws, preferred orientation of crystals, and other strain characteristics. It is used to determine unit cell dimensions as well as identify phases in crystalline material. For XRD analysis of our materials, we utilized the Bruker D8 Advanced (Germany) equipment. A recorder receives the peak location and intensities of dispersed rays, and a diffraction pattern is shown, which aids in identifying the identity and structure of crystalline substances. It operates by using constructive interference between two monochromatic parallel x-rays. The incident X-rays strike the sample and undergo constructive interference if satisfy Bragg`s law. The Bragg`s law is given as:

$$n\lambda = 2dSin\theta \qquad \text{eq. (3.1)}$$

Where $\lambda$ denotes the wavelength of incident rays, $d$ interplanar spacing and θ shows the angle of incidence. Furthermore, we can measure crystallite size of particles via appropriate analysis of X-ray line broadening. The formula below is used to calculate crystallite size D of any materials in nanometers with the aid of XRD peaks [10]:

$$D = \frac{0.9 \times \lambda}{\mathrm{d\ Sin\theta}} Sin\theta \qquad \text{eq. (3.2)}$$

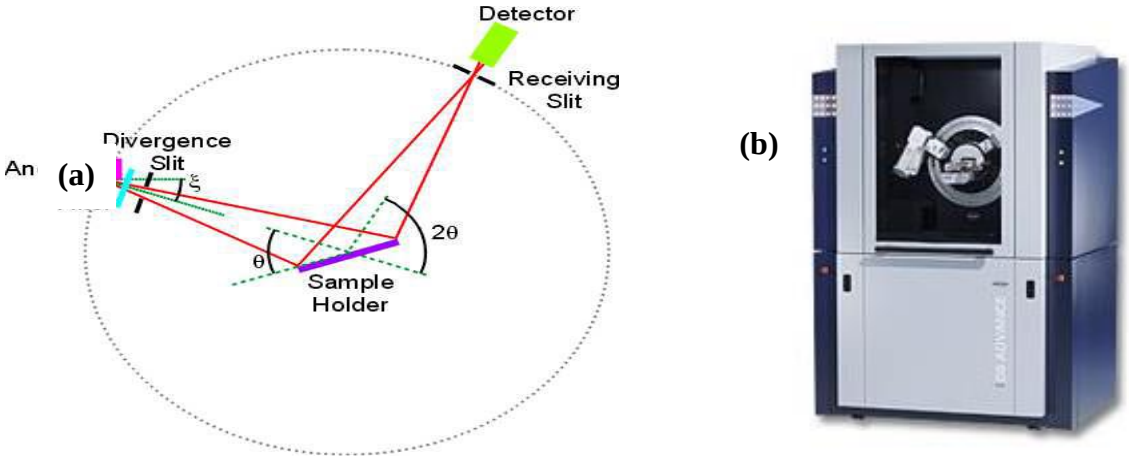


***Fig. 3. 3:*** (a) Schematic illustration of working of X-ray diffractometer [11] and (b) image of BRUKER D8 Advance instrument used for XRD analysis of samples.

### 3.2.2 Scanning Electron Microscope

This method provides useful information about the sample's microstructures. The model we used for SEM imaging was the Vega 3 Tescan (Czech Republic). SEM imaging is regarded as an essential component of material characterization of prepared samples since it gives informative information on catalyst shape and structural flaws, thus validating material characteristics verified by other analytical methods. SEM imaging may also confirm structural differences, topological alterations, and material deterioration. The SEM picture we receive is determined by how we utilize the detector that captures backscattered electrons. When an electron beam strikes a sample, it provides information on the texture, morphology, crystallinity, and orientation of the constituent materials. Its functioning mechanism begins when an electron cannon produces an electron beam, which travels through a sequence of electromagnetic lenses. These lenses aid in the

convergence of the beam on the sample. Some samples may need to be further prepared before they can be examined. These include metallography of metallic materials for high-quality images, sputtering of non-conducting samples with a conductive substance, and dehydration of biological samples [12, 13]. Fig. 3.4 depicts a schematic overview of the operation of a scanning electron microscope [14] as well as a picture of a commercial VEGA3 TESCAN equipment used for sample analysis.

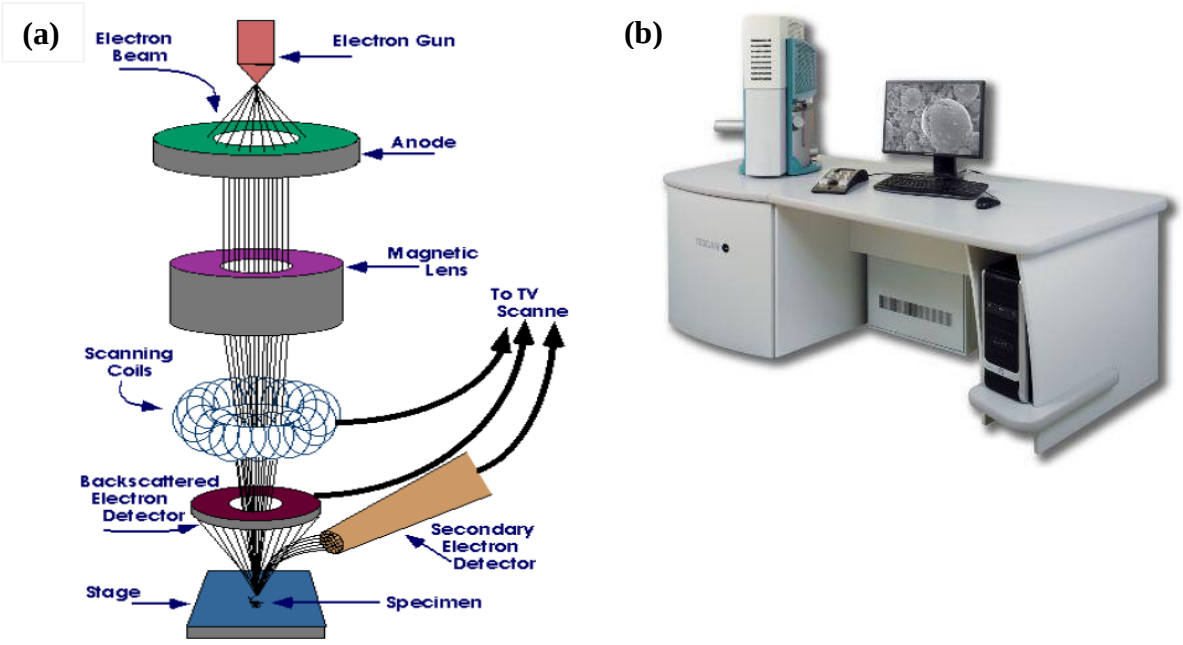


***Fig. 3. 4:*** (a) Diagram of working of a scanning electron microscope [14] and (b) Picture of commercial VEGA3 TESCAN instrument used for the analysis of samples.

### 3.2.3 Energy Dispersive Spectroscopy (EDS)

For the investigation of the chemical and elemental composition of elements with atomic numbers more than 3, it is a non-destructive analytical method. As the sample is blasted with electrons of high energy, it detects the distinctive x-rays that each element produces. The elemental composition of the targeted sample is shown on top of the enlarged picture of the sample using x-ray mapping.

The Oxford EDX detector was the model we utilised for EDS. EDS/EDX use SEM or TEM imaging to reveal the elemental makeup of the material. It operates on the

fundamental concept of each element having its own unique X-ray. As a result, when the sample is attacked with high energy electrons, the atoms on the sample's surface expel their electrons, resulting in the formation of vacancies in the structure. Due to the energy difference between the two electronic sites, these vacancies are subsequently filled by electrons from higher energy states, resulting in the emission of x-rays. The EDS detector captures the many x-rays emitted by the material, resulting in an EDS spectrum [15].

### 3.2.4 Fourier Transform Infrared Spectroscopy

Fourier transform infrared spectroscopy (FTIR) uses mathematical signal processing to turn raw data into the distinctive spectrum of the item being studied. According to general principles, the absorptance or transmittance of infrared radiation incident on the sample is measured in relation to the frequency range in which the functional groups contained in the sample vibrate. These vibrational frequencies are characteristics of functional groups, allowing them to be detected and distinguished from one another. The particular chemical groups present in the sample will be identified using spectrum data in the automated spectroscopy software [16] based on the infrared absorption frequency range 600-4000 cm1. It is a non-destructive qualitative analytical method in which various frequencies of radiation are shone on the sample and, based on the absorption, molecules exhibit vibrations that are inferred into a spectrum. We utilized the Agilent Technologies CARY 630 FTIR in the IR spectral region of 650-4000 $cm^{-1}$ to identify different kinds of organic bonding in solid materials. The vibrational frequencies measured in specific IR bands aid in the detection of organic moieties present within the framework. Fig. 3.5 depicts a schematic of the operation of a Fourier Transform IR spectrometer [17] as well as an image of an Agilent Technologies CARY 630 FTIR utilized for sample analysis.

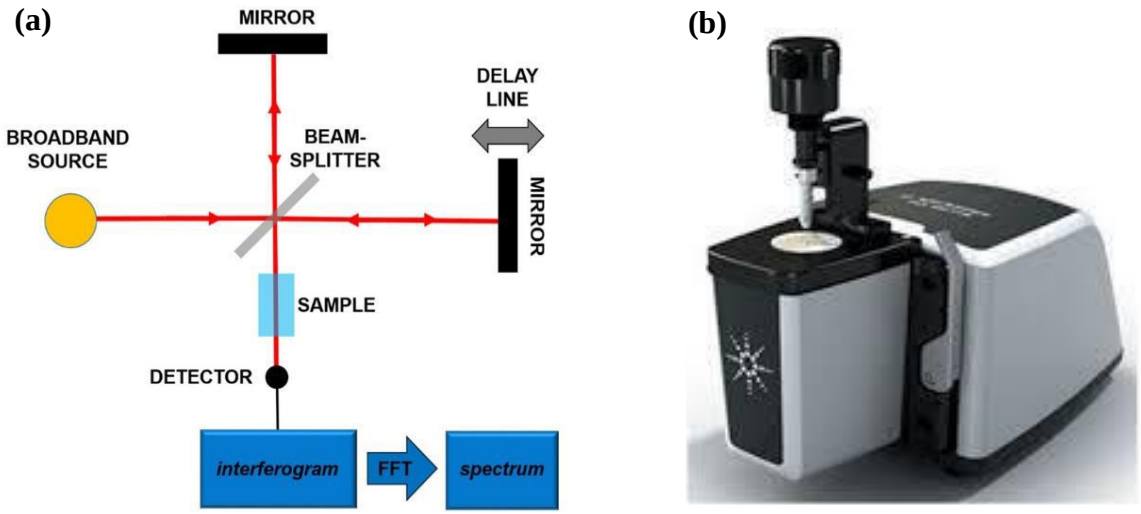


***Fig. 3. 5:*** (a) Working of a Fourier Transform IR spectrometer [17] and (b) Figure of CARY 630 FTIR by Agilent Technologies used for the analysis of samples.

### 3.2.5 Thermogravimetric Analysis

Thermogravimetric Analysis (TGA) is a destructive analytical method that measures the weight loss of a sample over a defined time period and over a broad range of temperatures. With this method, we may determine a variety of information about the sample, including enthalpy changes, reaction types and the rate of redox reactions, as well as temperatures for decomposition as well as melting, sub Physical phenomena such as phase shifts, absorption, adsorption, and desorption, as well as chemical phenomena including chemisorption, thermal breakdown and redox reactions, may be studied using this measuring technique Changes in temperature and weight of the sample are measured as a function of time. Thermal gravimetric analysis uses mass, temperature and time as its main measures, but it may also provide extra information that helps us understand physical and chemical changes that occur as temperatures rise. Thermogravimetric analysis (TGA) may be used to determine For example, just seeing that there is no loss indicates that the phase has thermal stability, which may be significant when trying to determine the suit If there is no mass shift, the TGA curve has a zero slope. TGA may also be used to determine a material's maximum operating Materials begin to degrade at this temperature. The TGA curve of a material is derived from the weight profile of a material as it is heated. The data

is collected as a weight % on the y-axis and temperature or time on the x- thermally related It is possible to determine sites of inflection for various chemical transformations by using the first order differential of the TGA curve [18]. A thermogravimetric analyzer [19] is shown schematically in Fig. 3.6, along with an illustration of the Discovery 5500, which is utilized for the examination of samples.

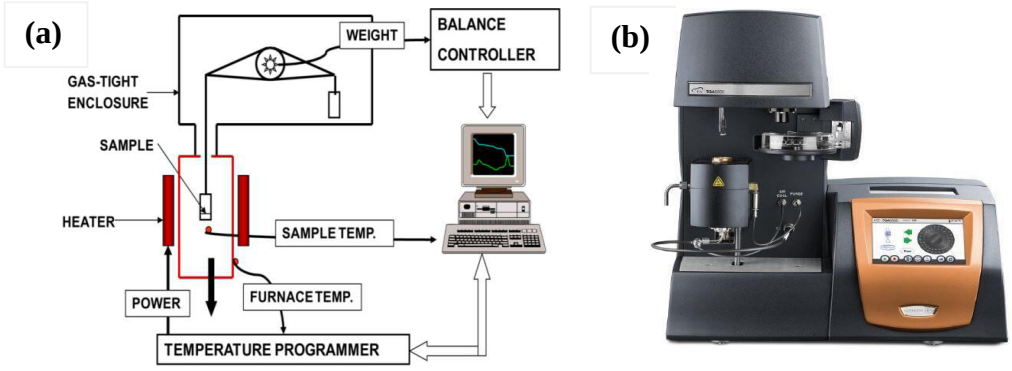


***Fig. 3. 6:*** (a) Schematic diagram of basic working of thermogravimetric analyzer [19] and (b) figure of Discovery 5500 by TA Instruments used for the analysis of samples.

### 3.2.6 Surface Area and Pore Size distribution Analysis

The surface area and porosity of a material's structure significantly influence its behavior and performance in a given application This may be ascribed to their distinct physical characteristics of particular region and pores. One of the most important analyses we do on a useful material is the surface area determination, which is regarded fundamental information regarding materials appropriate for electrocatalytic BET is a widely recognized technique for calculating surface area of materials based on the quantity of adsorbate adsorbed by material relative to partial pressure, among other ways. As a common adsorbate, nitrogen is employed in the BET technique at 77 K, which is the boiling point of nitrogen. Adsorption of nitrogen by a solid molecular layer of material results in a particular region of material. When using the BET technique, nitrogen is trapped in pore spaces and layers. This technique may be used to evaluate a wide variety of porous materials, from macro porous to meso porous is most often measured using the BJH technique, which ignores the sample's exterior surface area when calculating pore size distribution (pore size, volume, and surface area).

## 3.3 Electrochemical Measurements

To determine the electrochemical characteristics of the samples, we employed cyclic voltammetry, electrochemical impedance spectroscopy, and linear sweep voltammetry, among others.

### 3.3.1 Cyclic Voltammetry

It is the analysis that aids in the study of the fundamental mechanism of an electrochemical reaction and the observed redox potential in order to evaluate redox couplings and sweep the voltage cyclically between the adjusted voltages. When performing this study, the electrolyte employed must possess certain characteristics that will not interfere with the analysis [20]. It is not permitted to decompose. The potential against a sweeping voltage is measured. The potential of current shows the precise location of the response. Here, the voltage V1 and V2 are alternately swept between two fixed rates, which are V1 and V2. Fig. 3.7 illustrates a typical cyclic voltammogram with distinct oxidation peaks.

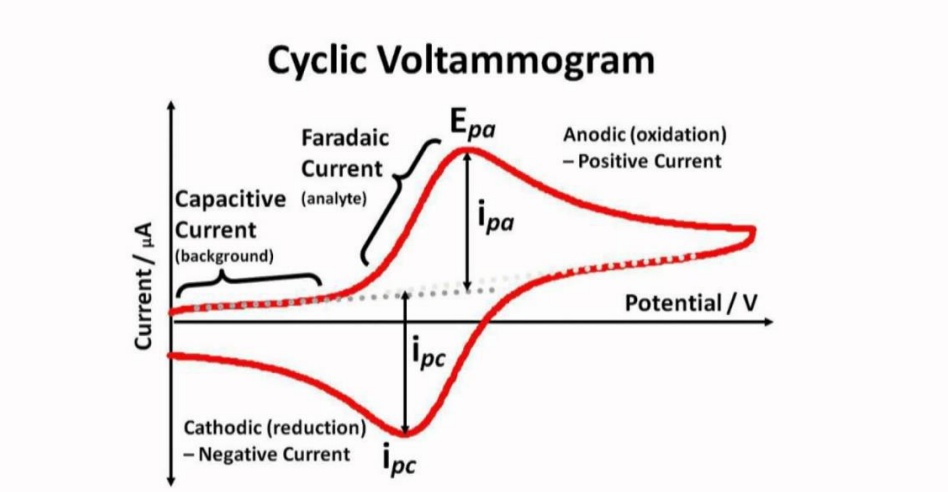


***Fig. 3. 7:*** Typical Cyclic voltammogram encountered in electrochemical studies.

### 3.3.2 Chronoamperometry

It is a well-known electrochemical analytical method for evaluating short-term stability and current density retention over a constant applied voltage, resulting in a current versus time graph. It is possible to get faradaic current produced by stepping voltage on

the catalyst-loaded working electrode, which can then be plotted against time. The applied voltage may be either single or double step, and a connection between faradaic current and experimental time is established in this study. It offers preliminary evidence of redox species produced by matching reduction and oxidation peak currents. It demonstrates a general upward trend in current generation, which is mostly due to the transfer of electrons in faradaic processes. It is possible to produce better signals with less noise interruption when chronoamperometry is conducted for a longer period of time [21].

### 3.3.3 Electrochemical Impedance Spectroscopy (EIS):

In addition to characterization of corrosion behavior, it also gives adequate information on the kinetics of the reaction [22], which is another electrochemical measuring analysis. When doing EIS testing, the following procedure is followed. It contains three electrodes, one for reference, one for counter, and one for our sample, all of which are dip in the same electrolyte. This analysis assists in the determination of impedance as well as the study of alternating current resistivity, conductivity, and inductivity. The continuous EIS measurement helps in understanding the long-term impact of an electrode in a known electrolyte, as well as measures of resistance to conductivity. Its output may be shown in a variety of graphs, including the Bode plot and the Nyquist plot.

## Summary

Various synthesis techniques for the production of metal organic frameworks have been discussed in this chapter. Analytical instruments for material characterisation, such as XRD, SEM, TGA, FTIR, BET surface analyzer, and EIS, have been briefly described in terms of operating principles and how these analytical methods may aid our research. Electrochemical measuring methods such as CV, chronoamperometry, and EIS have also been briefly addressed.

## References


[1] J. Gascon (Ed.), "Metal Organic Frameworks as Heterogeneous Catalysts," *Royal Society of Chemistry,* 2013.

[2] N. Stock, S. Biswas, "Synthesis of metal-organic frameworks (MOFs): Routes to various MOF topologies, morphologies, and composites," *Chem. Rev.,* no. 112 , pp. 933- 969, 2012.

[3] D.J. Tranchemontagne, J.R. Hunt, O.M. Yaghi, "Room temperature synthesis of metalorganic frameworks: MOF-5, MOF-74, MOF-177, MOF-199, and IRMOF-0," *Tetrahedron,* no. 64, pp. 8553-8557, 2008.

[4] L. Huang, H. Wang, J. Chen, Z. Wang, J. Sun, D. Zhao, Y. Yan, "Synthesis, morphology control, and properties of porous metal–organic coordination polymers," *Micropor. Mesopor. Mater.,* no. 58, pp. 105-114, 2003.

[5] K.S. Park, Z. Ni A.P. Côté, J.Y. Choi, R. Huang, F.J. Uribe-Romo, H.K. Chae, M. O'Keeffe, O.M. Yaghi, "Exceptional chemical and thermal stability of zeolitic imidazolate frameworks," *PNAS,* no. 103, pp. 10186-10191, 2006.

[6] X.-C. Huang, Y.-Y. Lin, J.-P. Zhang, X.-M. Chen, "Ligand-directed strategy for zeolite-type metal–organic frameworks: zinc (II) imidazolates with unusual zeolitic topologies," *Angew. Chem. ,* no. 45, pp. 1557-1559, 2006.

[7] J. Li, S. Cheng, Q. Zhao, P. Long, J. Dong, "Synthesis and hydrogen-storage behavior of metal-organic framework MOF-5," *Int. J. Hydrog. Energy,* no. 34, pp. 1377-1382, 2009.

[8] S. Brunauer, P.H. Emmett, E. Teller, "Adsorption of gases in multimolecular layers," *J. Am. Chem. Soc.,* no. 60, pp. 309-319, 1938.

[9] J.H. Cavka, S. Jakobsen, U. Olsbye, N. Guillou, C. Lamberti, S. Bordiga, K.P. Lillerud, "A new zirconium inorganic building brick forming metal organic frameworks with exceptional stability," *J. Am. Chem. Soc.,* no. 130, pp. 13850-13851, 2008.

[10] B. Howard, F.M. Murdie, C.M. Kloise, H. K. Boris, W. Wmiij-ni, C.R. Hubbard, "Standard X-Ray diffraction powder patterns from the JCPDS research associateship," *Int. Cent. Diffr. Data,* no. 1, pp. 265-275, 1986.

[11] Instrument X-ray Optics, Reflection Geometry, http://pd.chem.ucl.ac.uk/pdnn/inst1/optics1.htm.

[12] S.S. Afanasyev, T.V. Kychkina, L.N. Savvinova, "Scanning electron microscope (advantages and disadvantages)," *Colloquium-journal No. 2*, no. 2, 2019.

[13] J.I. Goldstein, D.E. Newbury, J.R. Michael, N.W. Ritchie, J.H.J. Scott, D.C.D. Joy, "Scanning Electron Microscopy and X-ray microanalysis," *Springer*, 2017.

[14] "Lawrence Livermore Radiation Safety Regulation, App. B, Summary of Radiation Generating Devices," *Radiation Safety Requirements.*

[15] "Introduction to Energy Dispersive X-ray Spectrometry (EDS)," pp. 1-12.

[16] P.M. Shameer, P.M. Nishath, "Exploration and enhancement on fuel stability of biodiesel: A step forward in the track of global commercialization," *Adv. Biofuels*, pp. 181-213, 2019.

[17] B. Patrizi, M.S. de Cumis, S. Viciani, F. D'Amato, "Dioxin and related compound detection: Perspectives for optical monitoring," *Int. J. Mol. Sci.*, no. 20, p. 2671, 2019.

[18] A.W. Coats, J.P. Redfern, "Thermogravimetric analysis. A review," *Analyst*, no. 88, pp. 906-924., 1963.

[19] P. Missak, "Infiltration growth processing of YBCO nano-composites: Shape forming, microstructural and magnetic studies".

[20] N. Aristov, A. Habekost, "Cyclic voltammetry-A versatile electrochemical method investigating electron transfer processes," *World J. Chem. Educ.*, no. 3, pp. 115-119, 2015.

[21] P. Kissinger, R.H. William, "Laboratory Techniques in Electroanalytical Chemistry," vol. second ed., 1996.

[22] "A. Sacco, Electrochemical impedance spectroscopy: Fundamentals and application in dye-sensitized solar cells," *Renew. Sustain. Energy Rev.*, no. 79, p. 814–829, 2017.

# Chapter 4

# Experimental

We used a solvothermal strategy to synthesize Mn-doped Zn-N-C@rGO (Mn/Zn-N-C@rGO) nanocomposite due to its benefits of high controllability, durability, scalable and consistent product, and homogenous distribution allowed by solution phase manufacturing. To fabricate the nanocomposite, we prepared graphene oxide separately and used product finishing steps to ensure the graphene oxide was of high quality. In this section, we will go through in detail the various procedures involved in the synthesis of graphene oxide.

## 4.1 Synthesis of graphene oxide

Graphene oxide can be used as a remarkable building block to create two- and three-dimensional structures with a wide range of functions and morphological characteristics. Surface chemistries and inherent functional groups can help derived designs perform better in a variety of applications [1]. Numerous preparation techniques have been successfully used to create graphene-like materials (graphene, GO, and rGO), including the scotch-tape approach [2], epitaxial growth [3], chemical vapour deposition [4], organic synthesis [5], liquid-phase exfoliation [6], and chemical exfoliation [7]. Among these, chemical exfoliation has gained considerable attention from researchers focusing on large-scale production and use of composite materials in construction, since it enables the customization of functions for specific applications. This method of preparation is the most often used for the synthesis of graphene oxide due to its scalability, simplicity of the process, high density of oxygen functional groups, and large-scale manufacturing. This is commonly referred to as the oxidation-exfoliation-reduction process. Graphene oxide is synthesized by the oxidation of a graphite precursor that serves as a layered template. The oxidised layers are then segregated into distinct layers and

subjected to reduction in order to maintain a constant oxygen to carbon ratio. In general, a low oxygen to carbon ratio is favoured in the final rGO product.

Graphene oxide was first synthesised chemically in 1859, when graphite powder was oxidised with potassium chlorate ($KClO_3$) and fuming nitric acid ($HNO_3$). Because of the in situ evolution of chlorine dioxide ($ClO_2$) gas and the possibility of explosion, this approach poses major safety risks [8]. Hummer and Offeman [9] developed a more fast and safe approach employing sodium nitrate ($NaNO_3$), potassium permanganate ($KMnO_4$), and strong sulfuric acid [9]. This process required less time for oxidation, and no harmful fumes were produced. Marcano et al. recently developed a novel method for producing more planar GO by using the $KMnO_4$ reagent in acidic combinations of sulfuric and phosphoric acids [10]. Simple mechanical or ultrasonic vibrational energy can be used to disintegrate the stacked GO sheets created in this approach. As GO is generated from graphite that has been densely stacked, there are a number of elements that influence the structure of the final product. We can optimise the size of GO by varying the graphite type, the number of reagents, and the process length. GO sheets ranging in size from nanometers to micrometres may be produced in this manner. Similarly, changing the energy used during the exfoliation process can also change the number of sheets in an exfoliated product.

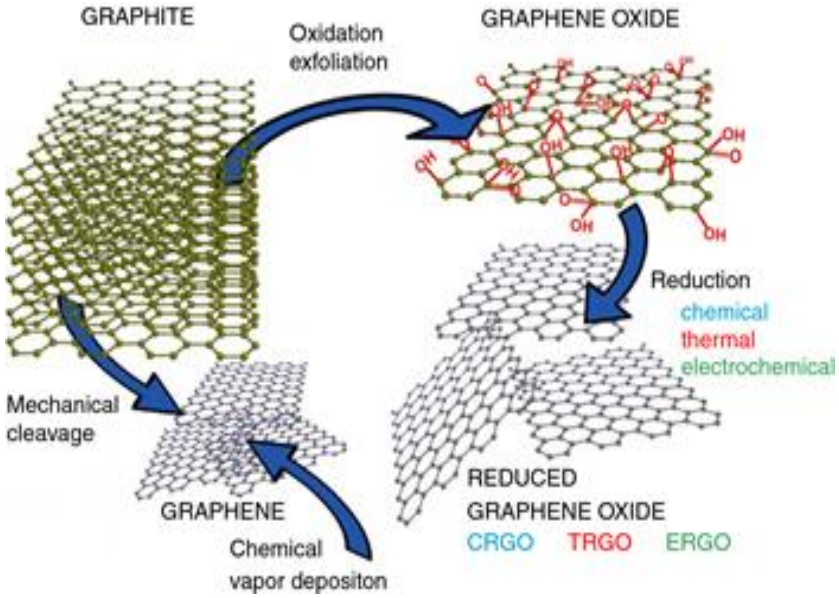


***Fig. 4. 1:*** Graphical illustration of chemical exfoliation method of GO [7]

## 4.2 GO Synthesis by improved Hummer's method

Improved Hummer's methodology has been adapted to synthesize graphene oxide with a few variations. Briefly, a mixture of 360mL of sulphuric acid ($H_2SO_4$) and 40mL of phosphoric acid (9:1) was stirred for more than a few minutes. Then, under stirring conditions, 2 g of graphite powder (1 wt% equivalent) was added to the mixed solution. In nine equal parts, 18 g of potassium permanganate ($KMnO_4$) (9 wt% equivalents) was gently added to the solution. After the addition of $KMnO_4$, the greenish-black color of the slurry begins to change into dark brown, and results in a modest exothermic reaction. The temperature of the reaction vessel was maintained between 35-40 $^oC$ by placing it in an ice bath. For extended oxidation, this mixture has been kept at 50 °C for 2 days (48 hours). When the reaction mixture was oxidized, it appears to be reddish-brown and was quenched with $H_2O_2$. This is known as chemical quenching, and it occurs when oxidation ends and the colour of the mixture changes to a light yellow.

As dense graphene oxide sheets dropped to the bottom of the beaker, the mixture sedimented into distinct layers. A large amount of deionized water was added to the clear, transparent acidic liquid, and the combination was allowed to settle. This procedure was repeated three times, followed by the addition of 100 mL of hydrochloric acid to the mixture, which dissolves manganese and other contaminants. Again, deionized water washing steps were performed until the pH of the solution reached neutral. The combination of deionized water and ethanol was centrifuged at a high speed (5000 rpm for 60 minutes). Once again, the dark brown result was centrifuged at 14000 rpm for 120 minutes under freezing conditions to ensure that no acid or solvent was present. In a vacuum oven, the washed product was dried overnight at 90°C. The GO produced after these washing stages is very layered and requires exfoliating before usage.

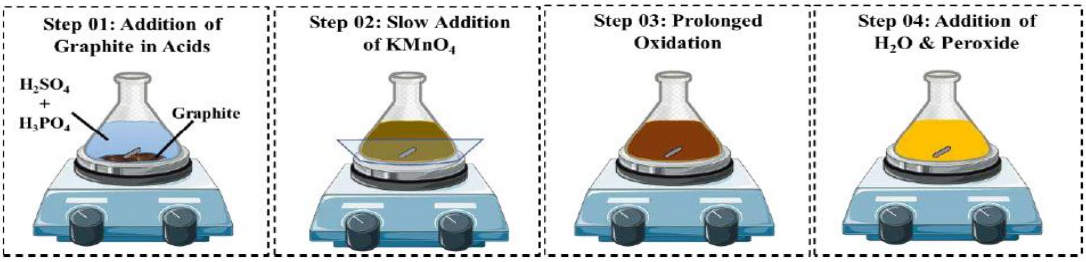


***Fig. 4. 2:*** Steps by step process of oxidation of graphite powder

## 4.3 Synthesis of Mn-doped ZIF-8 (Mn-ZIF-8) and Mn-doped Zn-N-C (Mn/Zn-N-C)

Manganese metal organic framework Mn-ZIF-8 was synthesized following solvothermal approach. Then, using a modified procedure, Mn-doped ZIF-8 was prepared with vigorous stirring, 1.66 g zinc nitrate hexahydrate ($Zn(NO_3)_2.6H_2O$ and 0.31g manganese nitrate hexahydrate ($Mn(NO_3)_2.6H_2O$ were completely dissolved in 80 mL N, N-dimethylformamide (DMF) to make a homogeneous solution (A). After that, 0.91 g of 2-Methylimidazole was dissolved in the DMF solution (B). After mixing A and B solutions, the reaction temperature was raised to 120°C in a 100 mL Teflon-lined stainless-steel autoclave and held for overnight at a temperature ramp of 3 $^oC\ min^{-1}$ to permit Mn-doped ZIF-8 nanocrystals to assemble. These Mn-ZIF-8 nanocrystals were separated by centrifugation after being cooled down to ambient temperature, washed three times with ethanol, and then dried for 6 hours at 80 °C in a vacuum oven.

Following that, the Mn-ZIF-8 particles were distributed in a ceramic boat and heated to 350 $^oC$ for 1.5 hours in a tube furnace. The temperature of the furnace is ramped up to 700°C at a rate of 3°C min-1 and then sustained for 3.5 hours. Then, the furnace is naturally cooled to normal temperature. The furnace is employed with Ar-$H_2$ flow (90/10 volume ratio) throughout the pyrolysis process. Carbon samples produced through this approach are designated as Mn-doped Zn-N-C (Mn/Zn-N-C).

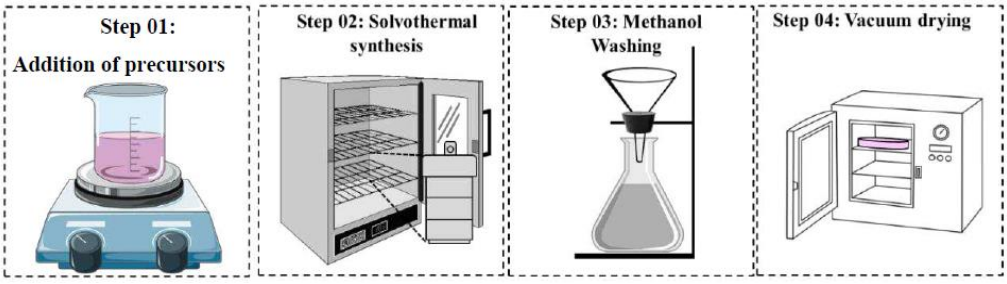


***Fig. 4. 3:*** Solvothermal synthesis of Mn-ZIF-8 MOF

## 4.4 Synthesis of Mn/Zn-N-C@rGO nanostructured composites

Different Mn/Zn-N-C@rGO nanocomposites (10%, 20%, and 30% GO) were synthesized by varying the quantity of GO templates used in the synthesis (see Fig. 4.4)

of the composite materials. Concisely, a certain quantity of GO was added to the DMF in accordance with the batch size of the Mn-doped ZIF-8 product and ultrasonicated for 2 hours to achieve uniform dispersion. The GO content in this dispersion was 22 mg/mL. Under vigorous stirring, zinc nitrate hexahydrate and manganese nitrate hexahydrate in a 5:1 molar concentration were dissolved in DMF, and the solution then added to 2-Methylimidazole dissolved in another DMF solution.

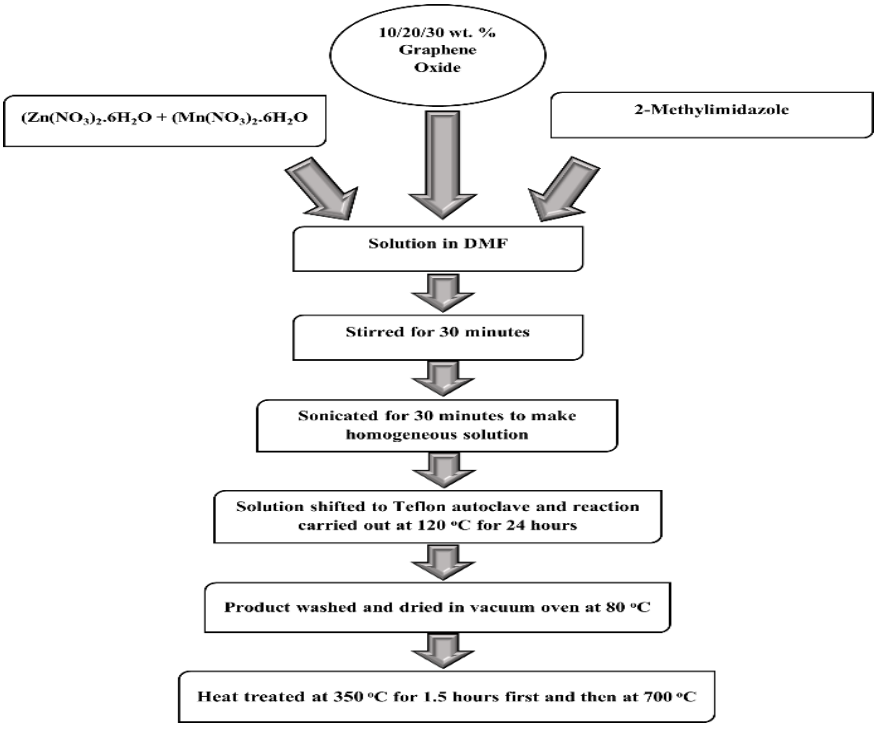


***Fig. 4. 4:*** Sequence of reaction steps in synthesis of Mn/Zn-N-C @30%rGO

The Mn-ZIF-8 precursor was present in the dispersion solution at a concentration of 36 mg per mL of solvent mixture. Afterward, the Mn-ZIF-8 precursor mixture was gradually added to the graphene oxide dispersion and ultrasonicated for some other 45 minutes. Then, the mixture was placed in an autoclave (Teflon lined) and heated to 120°C for 24 hours. Depending on the specific quantity of GO added, the color of the precipitates changed. Under vacuum at 80 $^{o}$C, crystals were recovered, cleaned, and dried. Centrifugation was used to collect the crystals, which were subsequently washed with ethanol and dried under vacuum at 80 $^{o}$C. The obtained solid was grounded for 15 minutes in the agate mortar pestle and then moved to an alumina boat for pyrolysis in an inert Ar-$H_2$ atmosphere within the tube furnace and maintained at the aforementioned conditions.

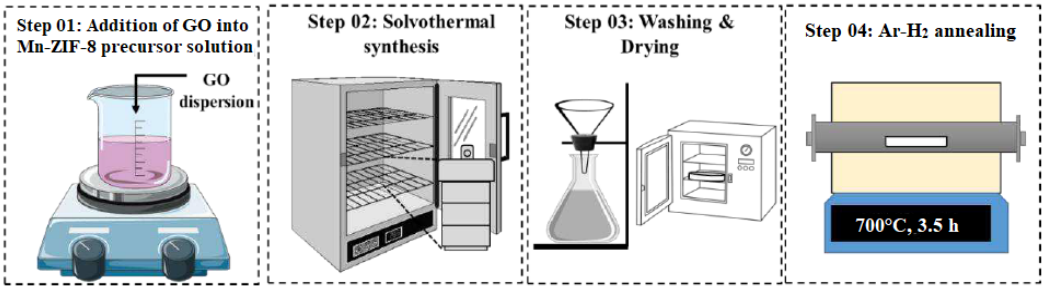


***Fig. 4. 5:*** Schematic illustration of preparation of Mn/Zn-N-C@rGO nanostructured composite

## 4.5 Material characterization and electrochemical measurement

Multiple material characterization methods were used to examine the prepared samples. Surface morphologies were attained by scanning electron microscope scanning images with an accelerating voltage of 20 kV using a TESCAN VEGA3 scan electron microscope. XRD patterns were attained using a Bruker Advance D8 X-ray Diffractometer along with emitted radiations (Cu Kα, P = 1200 W, I = 30 mA, V = 40 kV, and λ = 1.548) have been used to determine the crystalline phases of material. Discovery TGA 5500 by Thermogravimetric Analysis Instruments was used to obtain the thermogravimetric analysis (TGA) profiles of materials. The FTIR spectrum was produced by the CARY (630) FTIR Spectrometer was used to determine the different types of bonds present at the molecular level. The Brunauer–Emmet–Teller (BET) method was used to compute the surface area, whereas to determine the pore size distribution, we used the Barret–Joyner–Halinda (BJH) technique. Using the Quantachrome NovaWin instrument, we measured the $N_2$ adsorption-desorption isotherms of the as-prepared samples. The Raman spectra were obtained using a confocal Raman microscope (WiTech alpha R300) excited by a 532 nm Nd-YAG laser.

Catalyst ink was created for each sample prior to electrochemical tests, the catalyst (5 mg) was diluted in water/ethanol (5:1 v/v, 900 μL) and dissolved in Nafion solution (5 wt% in methanol, 50 μL) dispersed under 2 hours long ultrasonication to prepare a catalyst ink for the working electrode. A Bipotentiostat (CHI Model 760E) electrochemical workstation accompanied by a three−electrode cell along with rotating ring disc electrode (CHI Inc., RRDE-3A) assembly was used to record the electrochemical data. Platinum

wire and silver Ag/AgCl (3 M KCl) were used as the counter and reference electrodes, respectively, whereas the working electrodes were catalyst loaded GC and RDE. Glassy carbon (3 mm diameter, GC) as well as platinum rotating disc electrode (RDE) were polished with 0.05-micron, 0.3-micron, and 1.0-micron alumina slurries preceding to ink loading. To eliminate remaining alumina particles, the electrodes were ultrasonically cleaned in DI water. Accordingly, 10 μL of catalyst ink was drop casted onto the surface (loaded 0.385 mg $cm^{-2}$) of one electrode and then dried at 50 ºC for 15 minutes. For at least 30 minutes, very pure nitrogen or oxygen gas was flown through the electrolyte to achieve a nitrogen or oxygen saturated electrolyte solution before each measurement. To maintain nitrogen or oxygen saturation, a high-purity nitrogen and oxygen gas was bubbled across the electrolyte throughout the experiment. Alkaline electrolyte solution ($O_2$ saturated 0.1 M KOH) was used to conduct the ORR test, and cyclic voltammetry (CV) profiles were recorded at various scan speeds (5, 10, 15, 20, 25, and 50 mV/s) within a voltage window of 0.2 V to 1.2 V. Linear sweep voltammetry (LSV) measurements were performed at a scan rate of 10 mV $s^{-1}$ with various rotation rates (ranging from 100 to 2500 rpm). To examine the catalyst fuel cross over durability (methanol tolerance), methanol was introduced to 0.1 M KOH and CV was measured. EIS approach was used to calculate the resistance of solution by Nyquist plots from 0.1 Ω to 1 MΩ range at an amplitude of 0.005 V. The ORR measurements have been benchmarked using Pt/C commercial catalyst ink composed with the same method. All the potential values were expressed in terms of V vs RHE, as

$$E_{(RHE)} = E_{(Ag/AgCl)} + pH \times 0.059 + 0.210.$$

## Summary

In this chapter, experimental setup and methodology of preparation of manganese metal organic framework @ reduced graphene oxide composites (Mn-ZIF-8) have been discussed briefly. Additionally, the material's characterisation and electrochemical activity for oxygen reduction and evolution were discussed.

## References


[1] H. Bi, X. Xie, K. Yin, Y. Zhou, S. Wan, L. He, F. Xu, F. Banhart, L. Sun, R.S. Ruoff, "Spongy graphene as a highly efficient and recyclable sorbent for oils and organic solvents," *Adv. Funct. Mater.,* no. 22, pp. 4421-4425, 2012.

[2] K.E. Whitener Jr, P.E. Sheehan, "Graphene synthesis," *Diam. Relat. Mater.,* no. 46, pp. 25-34, 2014.

[3] P.W. Sutter, J.-I. Flege, E.A. Sutter, "Epitaxial graphene on ruthenium," *Nat. Mater.,* no. 7, pp. 406-411, 2008.

[4] C. Mattevi, H. Kim, M. Chhowalla, "A review of chemical vapour deposition of graphene on copper," *J. Mater. Chem.,* no. 21, pp. 3324-3334, 2011.

[5] J. Wu, W. Pisula, K. Müllen, "Graphenes as potential material for electronics," *Chem. Rev.,* no. 107, pp. 718-747, 2007.

[6] Y. Hernandez, V. Nicolosi, M. Lotya, F.M. Blighe, Z. Sun, S. De, I.T. McGovern, B. Holland, M. Byrne, Y. K. Gun'Ko, J.J. Boland, P. Niraj, G. Duesberg, S. Krishnamurthy, R. Goodhue, J. Hutchison, V. Scardaci, A.C. Ferrari, J.N. Coleman, Hernandez, "High-yield production of graphene by liquid-phase exfoliation of graphite," *Nat. Nanotechnol.,* no. 3, pp. 563-568, 2008.

[7] Rowley-Neale SJ, Randviir EP, Dena ASA, Banks CE., "An overview of recent applications of reduced graphene oxide as a basis of electroanalytical sensing platforms," *Appl Mater Today,* no. 10, p. 218–26, 2017.

[8] B. Brodie, *Phil. Trans. R. Soc. Lond,* no. 149, pp. 249-259, 1859.

[9] W. Hummers, R. Offeman, "Graphite oxide (GO) was prepared using the well-known Hummers method described by Hummers," *J. Am. Chem. Soc.,* no. 80, pp. 1339-1345, 1958.

[10] D.C. Marcano, D.V. Kosynkin, J.M. Berlin, A. Sinitskii, Z. Sun, A. Slesarev, L.B Alemany, W. Lu, J.M. Marcano, "Improved synthesis of graphene oxide," *ACS nano,* no. 4, pp. 4806-4814, 2010.

# Chapter 5

# Results and Discussion

## 5.1 XRD results

To determine the phases in the sample, XRD patterns of produced samples were used to identify peak positions at the diffraction angle and relative intensities. Information on crystallinity, crystallite size, and preferred orientation of atomic planes can be obtained from peak shapes, broadness, and intensity. Fig. 5.1 shows the XRD pattern of prepared samples. In Fig. 5.1(a) diffraction peaks for as-synthesized Mn-ZIF-8 correspond with PDF # 00-062-1030, confirming that the crystallization is of high purity According to the findings, the presence of $Mn^{2+}$ in the reaction medium during the formation of ZIF-8 crystals showed no structural changes, and after being doped with $Mn^{2+}$, ZIF-8 materials maintained their crystalline integrity [1]. The ionic size of $Mn^{2+}$ (0.80 Å) is just slightly greater than that of $Zn^{2+}$ (0.74 Å) in tetrahedral coordination, making it likely that the doping of ZIF-8 crystals with $Mn^{2+}$ does not disrupt the lattice structure. [2] The $2\theta$ values demonstrate that Mn-ZIF-8 cubic phases remained intact during the existence of GO. Strong peaks at $2\theta$ =18.00, 16.39, 14.65, 12.68, 10.35, and 7.31° correspond to planes (222), (310), (220), (211), (200), and (110), respectively, indicating that the prepared Mn-ZIF-8 has high crystallinity. As a result, Mn-ZIF-8 was effectively incorporated into the layers of GO while retaining its crystal structure. Furthermore, no other peaks of unknown contaminants were discovered in any sample. Calcination was used on solvothermal produced materials with two major specific goals:

I. Eliminate coordinated solvent molecules (primarily 2-methylimidazole) that were covalently linked to the manganese and zinc ions of the metal organic framework during the formation of the MOF coordination network. In order to conduct electrochemical testing, DMF molecules penetrate porous Mn-ZIF-8 structures and clog the pores that need to be activated. These solvent molecules degrade the adsorption sites and diffusional area of MOF, thereby impairing electrocatalytic activity. Using high temperatures in an inert atmosphere to

treat Mn-ZIF-8 completely eliminates the coordination of DMF solvent with metal ions and organic linker molecules, as well as the hydrogen bonding intermolecular interactions that occur between these molecules.

II. In Mn/Zn-N-C@rGO nanocomposite, reduced graphene oxide is composited with Mn/Zn-N-C@rGO. Due to the in situ high temperature and pressure conditions created by solvent vaporisation, as well as the presence of metal salts and organic molecules, solvothermal synthesis provides a strong reducing environment. However, the degree of reduction achieved is ordinary, and a dedicated reduction step is required to complete the reduction of GO into rGO.

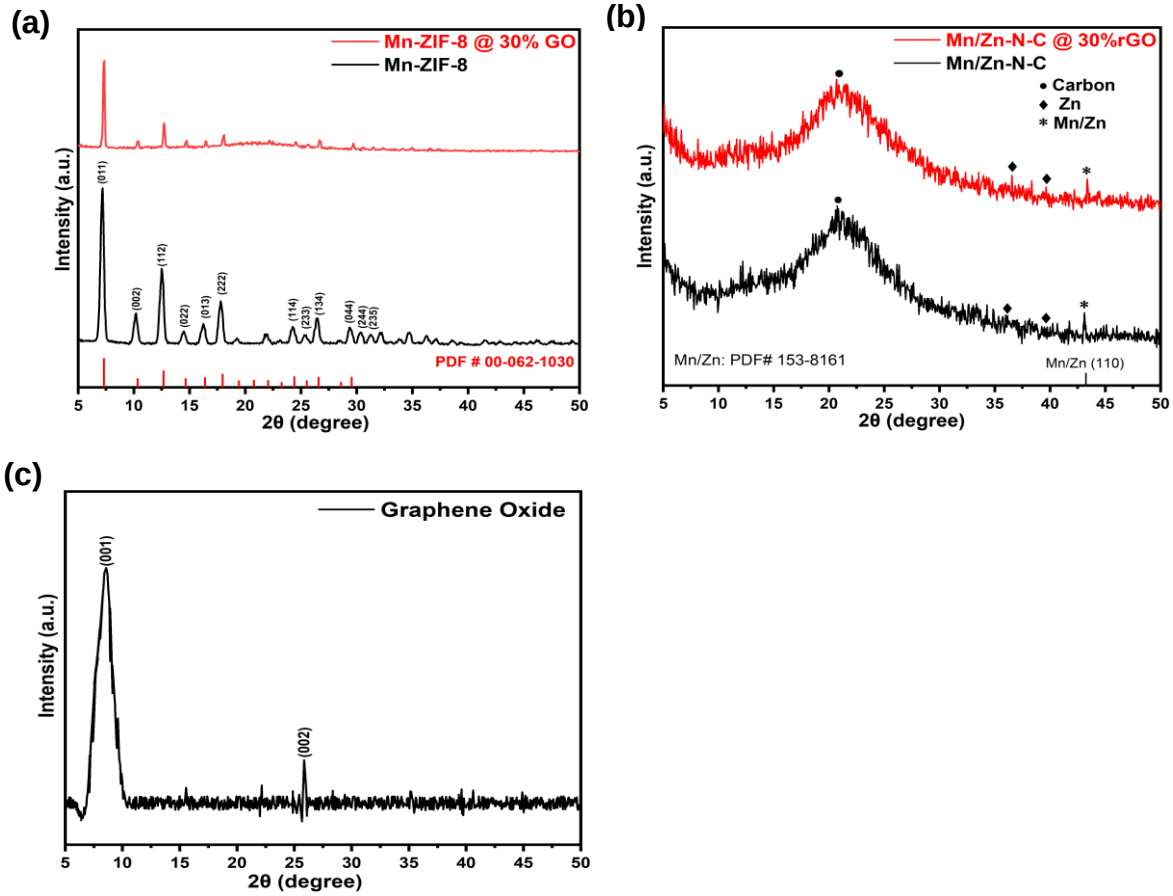


***Fig. 5.1:*** XRD patterns of (a) Mn-ZIF-8 (black), Mn-ZIF-8 @ 30% GO composite (red) along with the reference pattern of ZIF-8, (b) calcined sample of Mn/Zn-N-C @ 30%rGO (red) and Mn/Zn-N-C (black), (c) synthesized Graphene Oxide.

Thermal treatment in an inert atmosphere, which we utilized in our work, is a simple way of reducing GO.

The XRD pattern of an Mn/Zn-N-C and Mn/Zn-N-C @30% rGO is shown in Fig. 5.1(b). Calcination at 700 $^{O}$C for 3.5 hours in a continuous flow of Ar-$H_2$ mixture decomposes roughly bound and poorly coordinated linker (2-MeIM) molecules [3]. Peaks of Carbon, Zn, Mn/Zn phases have been indicated with dot (●), diamond (♦), and asterisk (*) signs respectively. Abroad peak at around 21° can be attributed to graphitic carbon in the pyrolyzed samples. When the synthesized sample is pyrolyzed at a high temperature, the peak at 21° becomes stronger, suggesting that the material has formed a more ordered graphitic structure. Furthermore, the XRD pattern of the Mn/Zn-N-C @30% rGO (red curve) sample is quite similar to the Mn/Zn-N-C pattern, with no other significant peaks observed. XRD pattern of GO (graphene oxide) is shown in Fig. 5.1(c). The formation of graphene oxide was confirmed by the angle 2θ of 9° that was referred to the (001) plane of oxidized graphite and existence of unexfoliated graphite is indicated by a less prominent peak at 2θ of 26.8 °, which corresponds to the (002) plane.

## 5.2 TGA results

Thermogravimetric analysis of Mn-ZIF-8 was performed to establish a thermal profile of the material, which aids in identifying physical and chemical changes that occur when a sample is heated in an inert gas environment. TGA of Mn-ZIF-8 was performed under an inert environment of nitrogen to better understand the carbonization of the compound is shown in Fig. 5.2. Before 400 $^{O}$C, there is no major weight loss occurs. More

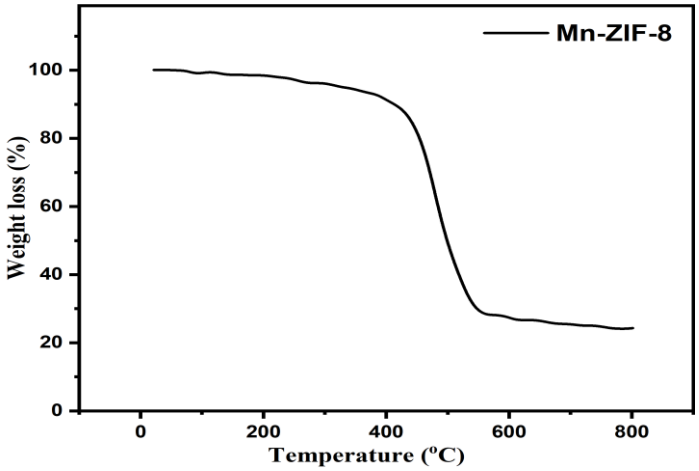


***Fig. 5.2:*** TGA curve of Mn-ZIF-8.

than 80% of the weight is lost between 400 $^{O}$C and 550 $^{O}$C, which is a critical step for rapid weight reduction. After 550 $^{O}$C, weight loss is negligible.

## 5.3 FTIR results

Fourier transform infrared spectra of prepared samples have been shown in Fig. 5.3. Fig. 5.3(a) shows the molecular patterns of GO, Mn-ZIF-8, and Mn-ZIF-8 @30% GO, which are all very remarkably comparable with the literature [4, 5]. GO reveals specific infrared (IR) frequency groups of C–O single bond, C–O–C bond, C–O–H bond, C=C double bond, and C=O double bonds appear at 1044 $cm^{-1}$, 1218 $cm^{-1}$, 1372 $cm^{-1}$, 1046 $cm^{-1}$, 1621 $cm^{-1}$, and 1724 $cm^{-1}$ respectively, corresponding to carbonyl and carboxyl groups.

These moieties are rarely found on the basal planes of graphene sheets but are widely present at the edges of 2D sheets. While O–H bond appears between 3200 $cm^{-1}$ and 3600 $cm^{-1}$ corresponding to an alcoholic hydroxyl group. The imidazole group is represented by three major frequency bands in Mn-ZIF-8. C=N bonds were corresponded by frequency bands at 1578 $cm^{-1}$, while bands at 1315 $cm^{-1}$ and 1152 $cm^{-1}$ emerge due to C–N bonds. The peaks identified at 754 $cm^{-1}$ and 680 $cm^{-1}$ correspond to Zn-O bonds and Zn-N bonds respectively, which confirm the growth of Mn-ZIF-8 on the GO sheet. The FTIR spectrum of Mn-ZIF-8@GO does not have a peak at 1724 $cm^{-1}$ that corresponds to C=O bonds of the carboxyl group, which shows that the carboxyl groups of GO interact with $Zn^{2+}$ [6]. FTIR spectra of annealed Mn/Zn-N-C and Mn/Zn-N-C @30% rGO nanocomposite (calcined) are shown in Fig. 5.3(b). It is worth mentioning that when Mn-ZIF-8 and Mn-ZIF-8@30% GO were calcined at 700 $^{O}$C in an inert environment, all the distinctive vibration bands vanished. After the Mn-ZIF-8 sample was calcined at 700 $^{O}$C under an Ar-$H_2$ environment, only weak and wide bands situated at around 1247 $cm^{-1}$ and 1053 $cm^{-1}$ represented the skeletal vibration of graphitic carbon and a significant number of oxygen-containing groups decomposed [7]. It was found that the carbonous species in samples of Mn/Zn-N-C and Mn/Zn-N-C@30% rGO had been extensively carbonized.

Hence, FTIR spectra confirm our interpretation that annealing at a high temperature result in the formation of an oxygen-deficient structure with an embedded structural defect suitable of delivering ephemeral and electrocatalytically active storage sites for reduction order.

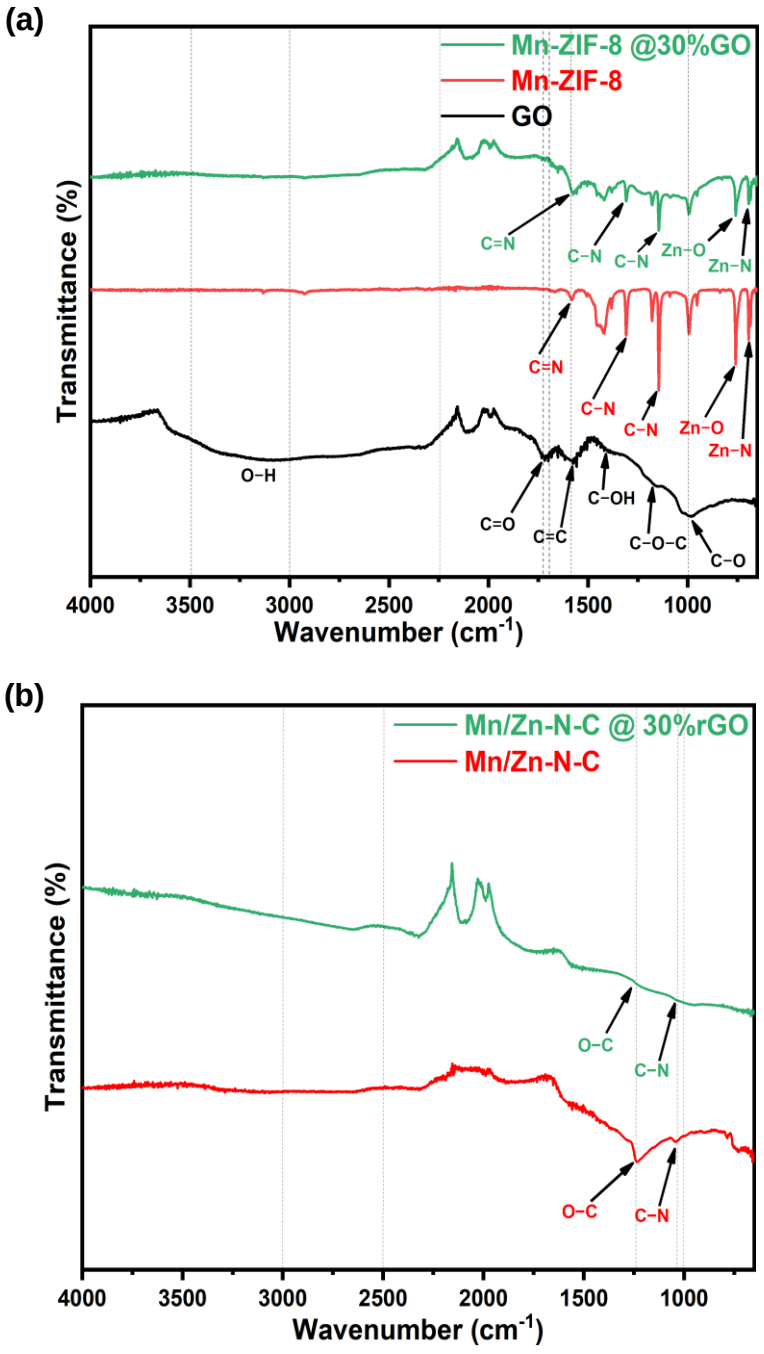


***Fig. 5.3:*** FTIR spectra of (a) Mn-ZIF-8 @30%GO (green), Mn-ZIF-8 (red), GO (black), (b) post calcination samples of Mn/Zn-N-C @30% rGO (green), Mn/Zn-N-C (red).

## 5.4 Surface area and porosity results

Specific surface areas and porosities were determined to determine the sample surface and pore parameters. For this purpose, the $N_2$ adsorption and desorption isotherms of samples were collected, and they were used to calculate surface areas using the BET technique and pore distribution using the Barrett-Joyner-Halenda method. The BET and BJH techniques

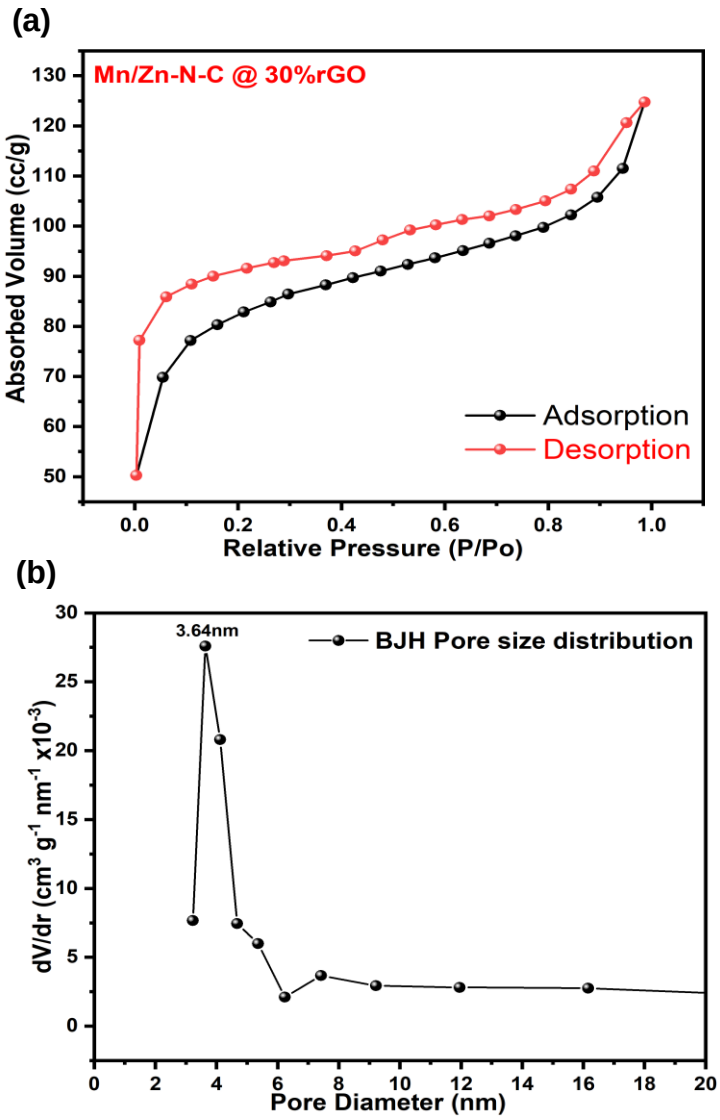


***Fig. 5.4:*** (a) BET nitrogen adsorption – desorption isotherm of Mn/Zn-N-C @30% rGO and (b) BJH pore size distribution curve of Mn/Zn-N-C @30% rGO.

are widely recognized as the most reliable methods for determining the surface and pore characteristics of nanoscale materials. Fig. 5.4(a) and (b) shows the $N_2$ adsorption-desorption isotherms, as well as BJH pore size distributions of Mn/Zn-N-C@30% rGO. For plots of pore size distribution, we adapted desorption segment of the isotherm, and these isotherms reflect type-IV hysteresis loops, confirming the existence of mesopores. The area contained by isotherms is very important since it reveals surface area information similar to the quantity of adsorbate (nitrogen at its boiling point of 77 K) absorbed by the material. Mn/Zn-N-C@30% rGO has a BET surface area of 383.318 $m^2/g$ and a pore volume of 0.061 $cm^3/g$. The pore size distribution of Mn/Zn-N-C@30% rGO calculated by BJH pore size distribution analysis indicates that it is within the mesoporous range (above 2 nm) between 2.5 and 5 nm. The large pore volume and surface area allow electrolytes to diffuse through the pores and attain maximum surface area. Furthermore, these favorable structural features could promote the interaction with reactants in catalysis.

## 5.5 SEM, EDS and TEM results

Morphology and structure of prepared samples were examined by scanning electron microscope. SEM micrographs of synthesized Mn/Zn-N-C, Mn/Zn-N-C @30% rGO, and Graphene Oxide are shown in Fig. 5.5, as well as an EDX analysis of Mn/Zn-N-C @30% rGO. Before pyrolysis, Mn-ZIF-8 possessed the ZIF-8 structure's inherited rhombic dodecahedral structure. The Mn-ZIF-8 partially decomposes during the pyrolysis when the unstable organic groups evaporate, leaving merely the nano porous carbon remaining. The Mn-ZIF-8 was turned into a black powder after pyrolysis subsequently the carbonization of the organic linker and transformed into a nano porous crystalline structure that did not have a regular and particular shape, as illustrated in Fig. 5.5(a–c). SEM images of Mn/Zn-N-C @30% rGO are shown in Fig. 5.5(d–f). It is obvious that particles are synthesized onto a GO template, and consequently no layer disturbance occurs during thermal reduction. It indicates that graphene oxide reduction through solvothermal synthesis resulted in enough depilated and aggregated GO sheets and that thermal reduction had no effect on the integrity of nanocomposite. Nanocomposite growth can be confirmed by the fact that the major objective of self-templated development has

been achieved by GO. Furthermore, microstructures of GO synthesized using an improved Hummer's method are depicted in Fig. 5.5(g–i). The comparative elemental analysis of Mn/Zn-N-C @30%rGO was performed using EDX spectroscopy, and the results are depicted in Fig. 5.5(j). Mn, Zn, C, and O were identified to be critical components. In this analysis, no detectable quantity of any impurity was found. Weight proportions of Mn, Zn, O, N and C are 0.2%, 11%, 12.5%, 13.8% and 62.5% respectively.

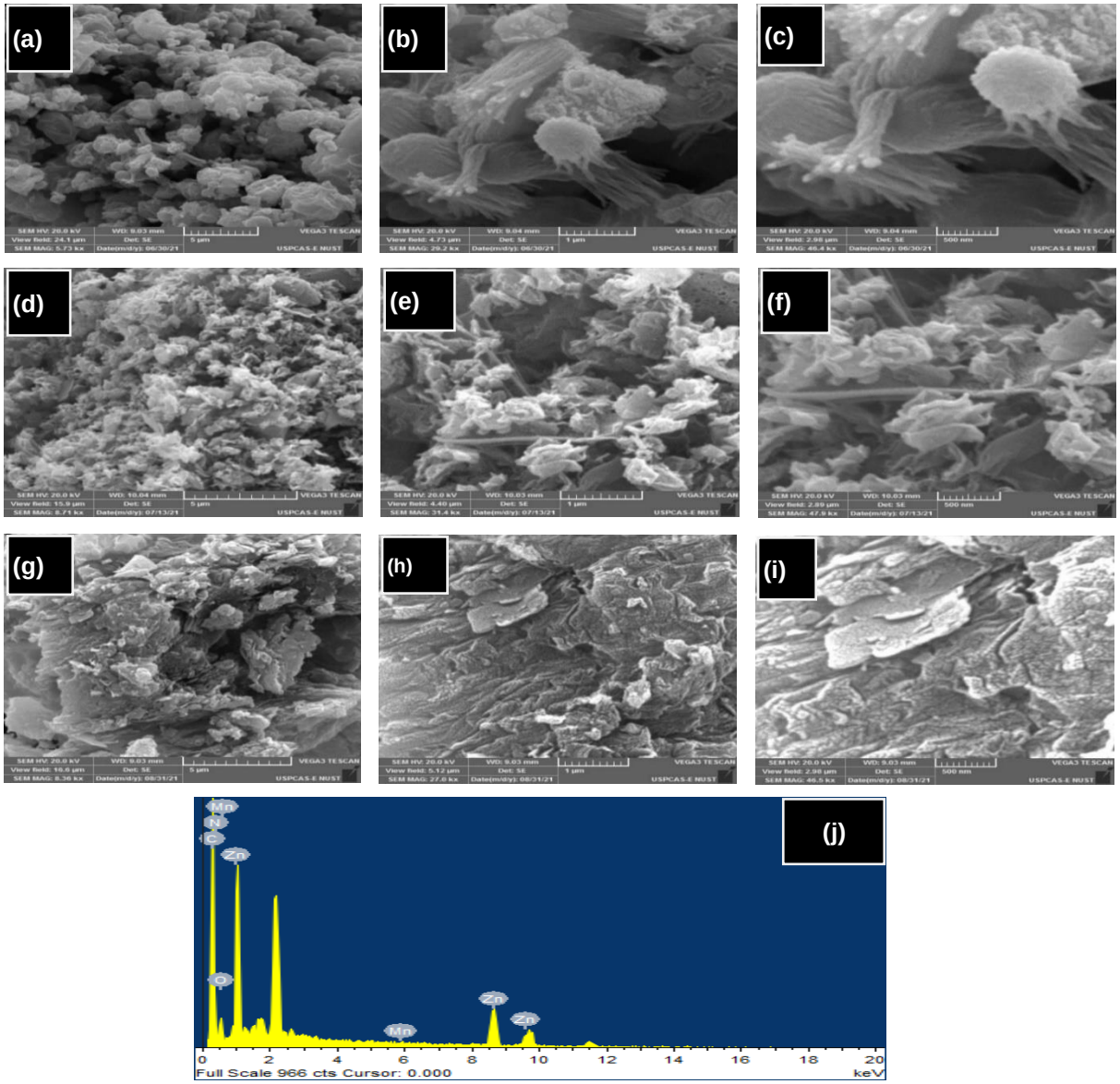


***Fig. 5.5:*** SEM images of (a-c) Mn/Zn-N-C, (d-f) Mn/Zn-N-C @30%rGO, (g-i) GO. EDX spectroscopy of (j) Mn/Zn-N-C @30%rGO

The structural features and shape of nanoparticles constituted of hard nanoparticles composed of metallic particles were observed using TEM. The Mn/Zn-N-C @30% rGO reveals the metal distribution on the backbone of reduced graphene oxide. As a result, the agglomeration of nanoparticles is reduced by the rGO nanosheets. Metal particles are evenly distributed on the rGO surface and are also deposited in the pores between them.

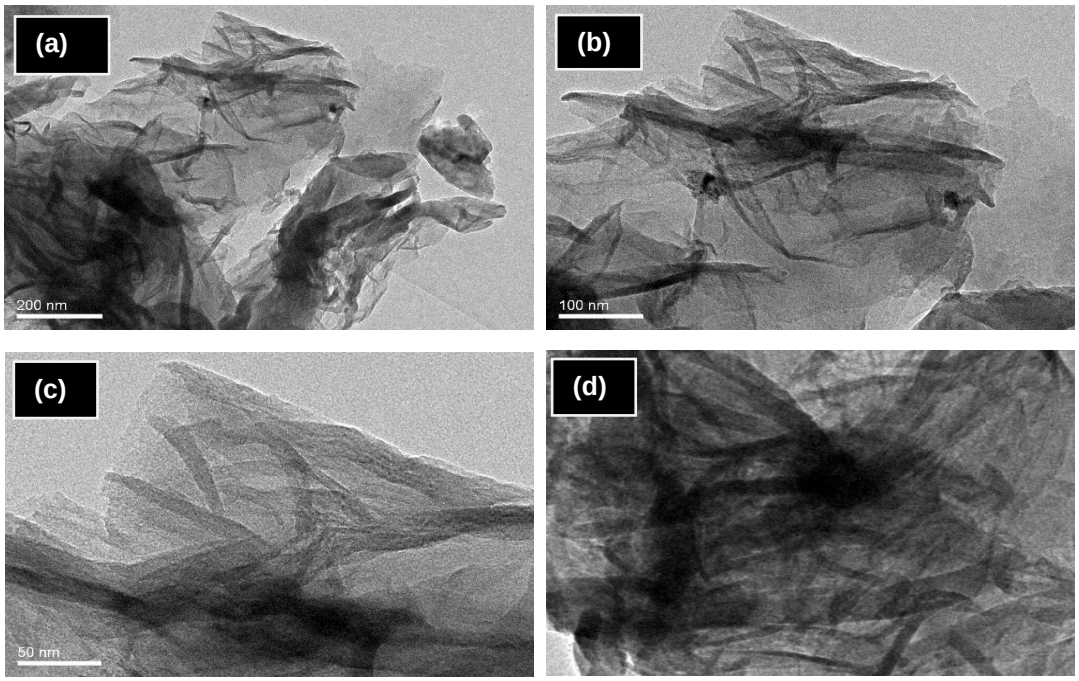


***Fig. 5.6:*** TEM images of Mn/Zn-N-C @30%rGO

## 5.6 XPS Results

Electrocatalyst constituents were also studied using XPS analysis of Mn/Zn-N-C @30% rGO to determine the surface elemental composition and the oxidation states. Fig. 5.7 (a) depicts the survey spectrum of the electrocatalyst, which revealed the existence of distinct peaks corresponding to the binding energies of Mn, Zn, O, N, and C elements in the electrocatalyst. Fig. 5.7 (b) shows the high-resolution spectra of Mn 2p, which has two prominent peaks at 652.74 and 640.88 eV split by 11.86 eV of spin-orbit and assigned to Mn $2p_{1/2}$ and Mn $2p_{3/2}$, respectively. Four subpeaks are formed by the deconvolution of the two main peaks. The binding energy of $Mn^{2+}$ is represented by the pair of subpeaks at 652.5 and 640.8 eV, while that of $Mn^{3+}$ is represented by the pair at 654.2 and 642.7 eV. Similarly, the Zn 2p fundamental XPS spectrum, as shown in Fig. 5.7 (c), has two peaks at 1044.5 eV and 1021.3 eV, which are caused by the Zn $2p_{1/2}$ and Zn $2p_{3/2}$ of tetrahedral $Zn^{2+}$, respectively. This shows that Zn is in the +2-oxidation state when it is in the Mn/Zn-N-C @30% rGO nanocomposite. The nitrogen group found on Mn/Zn-N-C @30% rGO in Fig. 5.7 (d) includes graphitic-N, pyrrolic-N, and pyridinic-N species, with binding

energies of 400.3, 398.4, and 397.8 eV, respectively. In Fig. 5.7 (e), the C 1s spectrum is subdivided into four peaks at 285.2, 284.3, and 283.7 eV. These peaks correspond to C-N, C=C, and C-C, respectively, and are shown in the figure. A small amount of oxidation caused by exposure to air may be responsible for the existence of the element O.

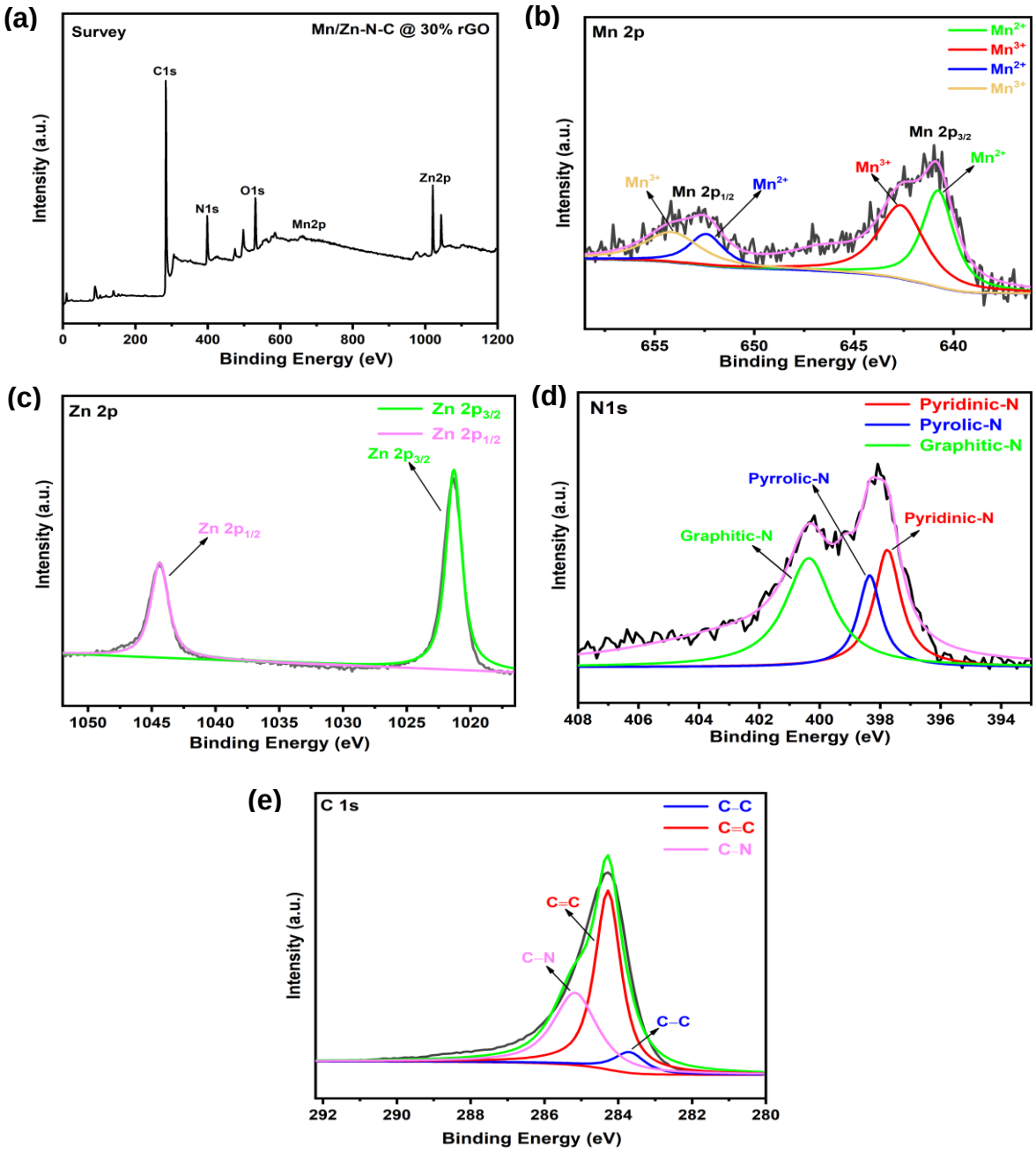


***Fig. 5.7:*** XPS spectra of Mn/Zn-N-C @30% rGO electrocatalyst. (a) XPS Survey spectrum. (b) Mn 2p detailed XPS spectrum. (c) Zn 2p detailed XPS spectrum. (d) N 1s detailed XPS spectrum. (e) C 1s detailed XPS spectrum with peak deconvolution.

## 5.7 Electrochemical measurement results

The performance of synthesized catalysts in oxygen reduction reactions was assessed using an electrochemical workstation with a rotating disc electrode assembly. For these experiments, the electrochemical cell we used had reference, counter, and working electrodes attached. Glassy carbon and revolving disc platinum electrodes were used to deposit catalyst ink independently. The surface of both working electrodes was polished with alumina slurry to eliminate any impurities or dust particles. After ink deposition, electrodes with catalyst were heated to 50°C in an electric oven to form a strong stiff layer. For electrochemical tests, a freshly produced 0.1M KOH aqueous solution was utilized as the electrolyte. The catalyst was tested using cyclic voltammetry in the following configuration. To remove entrapped air oxygen from the solution, pure nitrogen gas was purged through a prepared 0.1M KOH solution. All of the samples were subjected to CV testing to see whether any redox peaks appeared on the voltammogram. The electrolyte solution was then saturated with oxygen gas at a flow rate of three bubbles per second, which resulted in the electrolyte solution becoming completely saturated. For each sample, cyclic voltammetry testing revealed broad, noticeable reduction peaks.

Thereafter, detailed electrochemical tests were performed to precisely probe the ORR performance of each sample. A voltage range of 0.2–1.2 V was used for the cyclic voltammetry tests, which were conducted in an $N_2/O_2$ saturated 0.1 M KOH aqueous alkaline electrolyte solution. In Fig. 5.8(a), dotted and continuous lines represent cyclic voltammograms of Pt/C commercial, Mn/Zn-N-C @30% rGO, Mn/Zn-N-C @20% rGO, Mn/Zn-N-C @10% rGO, and Mn/Zn-N-C in $N_2$ and $O_2$ saturated 0.1 M KOH alkaline solutions, respectively. A pronounced oxygen reduction current peak in the $O_2$-saturated solution clearly confirms the existence of catalytic sites in the synthesized samples, in contrast to the plain CV curves in the $N_2$-saturated electrolyte. This reduction peak was found to correspond with the presence of ORR ($4H^+ + O_2 + 4e^- \rightarrow 2H_2O$) on the catalysts. As is well known, electrocatalytic activity is undoubtedly enhanced if a material has a higher reduction potential. ORR peak potentials of 0.58 V for Mn/Zn-N-C, 0.64 V for Mn/Zn-N-C @10% rGO, 0.65 V for Mn/Zn-N-C @20% rGO, 0.78 V for Mn/Zn-N-C @30% rGO, and 0.94 V for commercial Pt/C have comparatively shifted around further positive potentials, implying improved electrocatalytic performance as the quantity of

rGO increases. Though, Pt/C has the comparative ORR potential of all, demonstrating strong catalytic activity. It would be worth noting to declare that area under the CV curves increases accordingly with the increasing rGO concentration in the nanocomposite. The higher CV area leads to a larger specific capacitance, which shows that Mn/Zn-N-C @30% rGO catalysts have a superior solid-electrolyte interface due to notably larger BET surface areas.

The ORR performance of the catalysts is further investigated using linear sweep voltammetry (LSV). The linear sweep voltametric (LSV) responses of Mn/Zn-N-C, Mn/Zn-N-C nanocomposites (10, 20, 30% rGO), and commercial Pt/C coated GC electrodes in an $O_2$ saturated aqueous 0.1M KOH electrolyte at 1600 rpm rotation rate, shown in Fig. 5.8(b). As the oxygen reduction peak potential rises, the onset potential also rises with the same trend. This indicates that the activity of the ORR is improving with the corresponding rise in the rGO content.

A smaller Tafel slope confirmed the improved ORR catalytic activity of Mn/Zn-N-C @30% rGO, as shown in Fig. 5.8 (c). Tafel slope and Tafel plot are semi-quantitative parameters that provide an approximate estimate of the polarization behavior of an ORR catalyst. Electrode polarization is a frequent phenomenon in the ORR process, which is triggered by an increase in resistance. A high Tafel slope suggests that there would be significant overpotentials encountered during ORR, whereas a low Tafel slope predicts that there will be low overpotentials associated with obtaining higher current densities, indicating that ORR kinetics were more rapid. In Fig. 5.8 (c), the corresponding Tafel plots are also presented. The Tafel slopes of the Mn/Zn-N-C @30% rGO was noted to be 108 mV $dec^{-1}$, which was significantly lower than the Tafel plot slopes of commercial Pt/C (121 mV $dec^{-1}$), Mn/Zn-N-C @20% rGO (140 mV $dec^{-1}$), Mn/Zn-N-C @10% rGO (154 mV $dec^{-1}$) , and Mn/Zn-N-C (170 mV $dec^{-1}$). Based on the findings, the Mn/Zn-N-C @30% rGO outperformed the other catalyst samples in terms of kinetic reaction and electron transfer rate, as well as having the least over-potential concerns for ORR. Again, with increasing amounts of rGO, a gradual drop in slope values has been observed. In the order to determine the regularity of the ORR reduction potential, CV was conducted at the various scan rates (5–50 mV $s^{-1}$), and the outcomes are shown in Fig. 5.8 (d), suggesting that there has been no significant shift in the reduction peak. Peak current densities

increased with scan rate in the CV curves of Mn/Zn-N-C @30% rGO. This trend is concurrent with the Randle's–Sevcik equation, which states that the peak current and scan rate are directly proportional. of electroactivity on the electrode surface, causing significant current generation in CV. The LSV of Mn/Zn-N-C@30% rGO is shown in Fig. 5.9(a), together with measured half-wave and onset potential values. Tables 1 and 2, summaries the performance characteristics of ORR electrochemical activity for Mn/Zn-N-C, Mn/Zn-N-C@10% rGO, Mn/Zn-N-C@20% rGO, Mn/Zn-N-C@30%rGO, and commercial Pt/C catalysts.

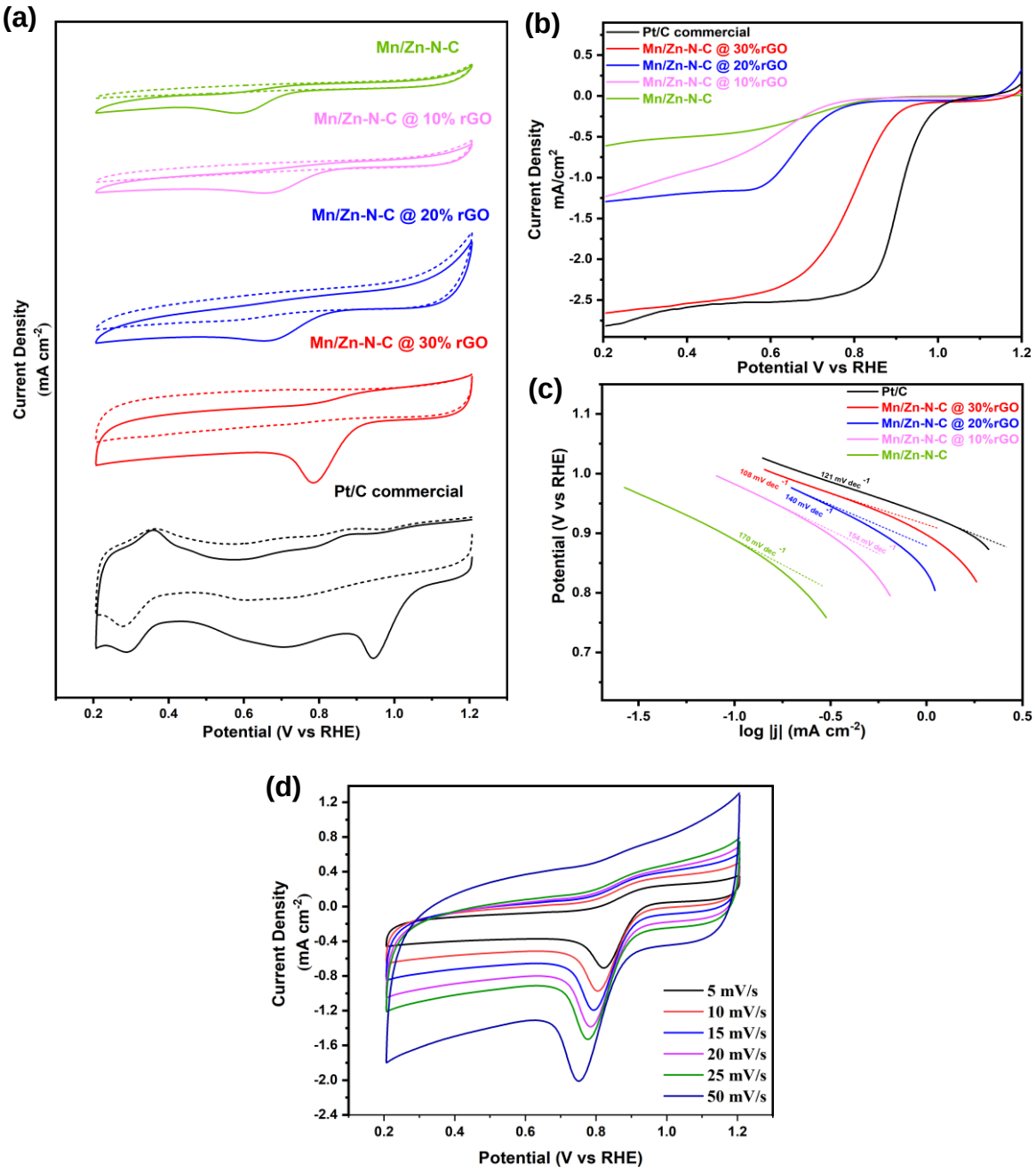


***Fig. 5.8:*** (a) Cyclic voltammetry profiles of Mn/Zn-N-C (green), Mn/Zn-N-C @10%rGO (magenta), Mn/Zn-N-C @20%rGO (blue), Mn/Zn-N-C @30%rGO (red) and Pt/C commercial (black) in $O_2$ (continuous line) and $N_2$ (dot line) saturated 0.1 M KOH solution. (b) Linear sweep voltammetry profiles of Mn/Zn-N-C (green), Mn/Zn-N-C @10%rGO (magenta), Mn/Zn-N-C @20%rGO (blue), Mn/Zn-N-C @30%rGO (red) and Pt/C commercial (black) in $O_2$ saturated 0.1 M KOH solution at 1600 rpm rotation with 10 mV $s^{-1}$ scan rate. (c) Tafel plots of Mn/Zn-N-C (green), Mn/Zn-N-C @10%rGO (magenta), Mn/Zn-N-C @20%rGO (blue), Mn/Zn-N-C @30%rGO (red) and Pt/C commercial (black). (d) Cyclic voltammetry profiles of Mn/Zn-N-C @30%rGO at different scan rates 5–50 mV $s^{-1}$ in $O_2$ saturated 0.1 M KOH solution.

Table 5.1: ORR peak potentials, peak current density and Tafel slope of synthesized samples

| Samples | $E_{pc}$ (V) | $J_{pc}$ (mA $cm^{-2}$) | Tafel slopes ($mVdec^{-1}$) |
|---|---|---|---|
| Pt/C | 0.94 | 1.72 | 121 |
| Mn-Zn-NC @ 30%rGO | 0.78 | 1.42 | 108 |
| Mn-Zn-NC @ 20%rGO | 0.65 | 0.76 | 140 |
| Mn-Zn-NC @ 10%rGO | 0.64 | 0.55 | 154 |
| Mn-Zn-NC | 0.58 | 0.51 | 170 |

To acquire a better understanding of the electroactivity of Mn/Zn-N-C@30%rGO, a sequence of LSV tests were executed on an 0.1 M KOH $O_2$-saturated electrolyte solution at varying rotating rates of RDE from 100–2500 rpm, as depicted in Fig. 5.9(b). Whereas onset potentials keep unchanged, diffusion limiting current rises as rotation rate increases, leading to enhanced mass diffusion at elevated speeds. Furthermore, higher rotating speeds lower the diffusion distance, increasing the current density even more.

Table 5.2: Comparison of onset potential, half-wave potential and maximum current density measured from LSV of synthesized samples

| Samples | $E_{onset}$ (V) | $E_{1/2}$ (V) | $J_{max}$ (mA $cm^{-2}$) |
|---|---|---|---|
| Pt/C | 1.03 | 0.89 | 2.85 |
| Mn-Zn-NC @ 30%rGO | 0.97 | 0.8 | 2.65 |
| Mn-Zn-NC @ 20%rGO | 0.85 | 0.69 | 1.28 |
| Mn-Zn-NC @ 10%rGO | 0.82 | 0.64 | 1.22 |
| Mn-Zn-NC | 0.91 | 0.68 | 0.61 |

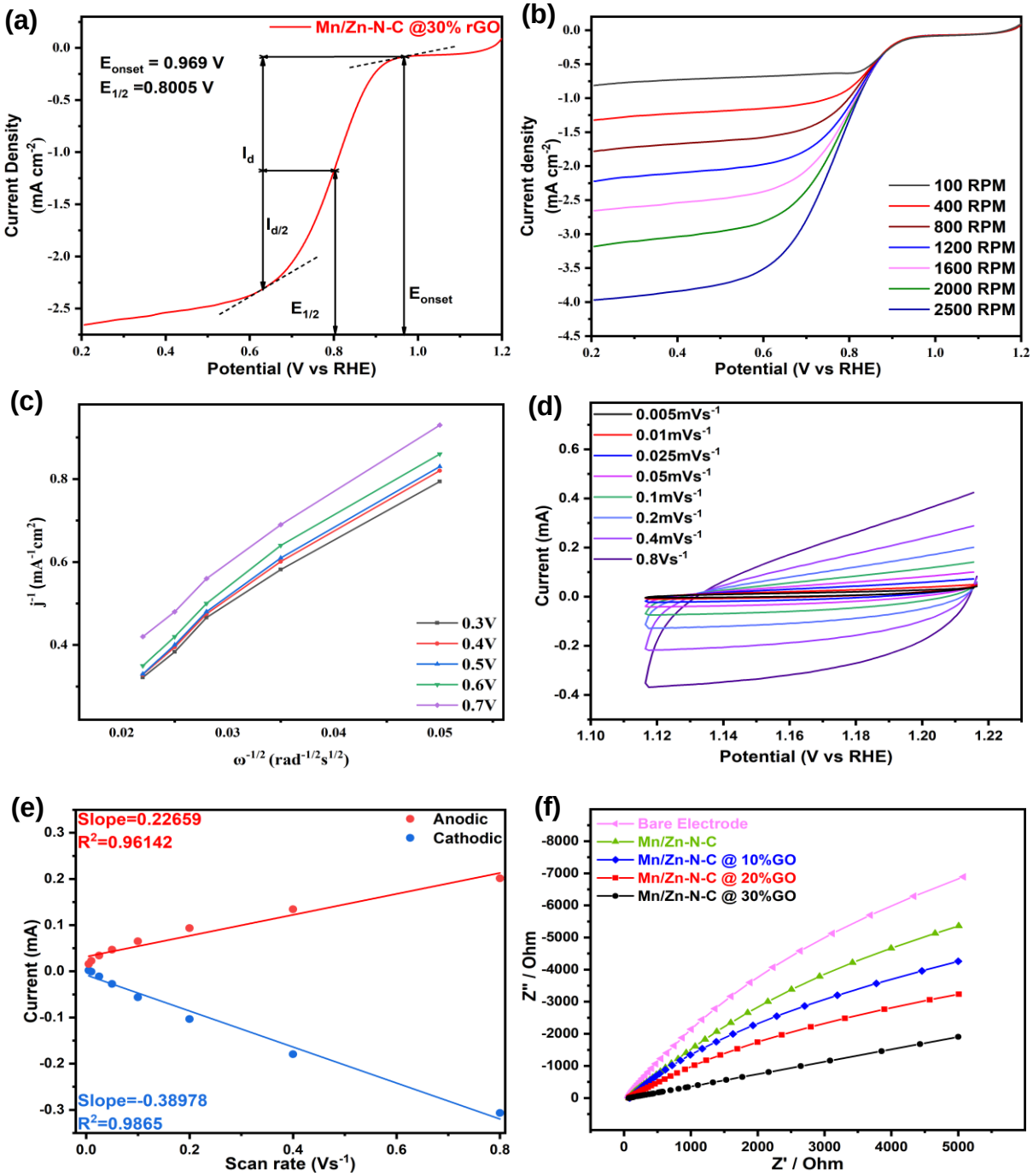


***Fig. 5.9:*** (a) LSV profile of Mn/Zn-N-C@30% rGO at 1600 rpm in $O_2$ saturated 0.1 M KOH with 10 mV $s^{-1}$ scan rate. (b) LSV profiles of Mn/Zn-N-C@30% rGO at different rotation speeds 100–2500 rpm with 10 mV $s^{-1}$ in $O_2$ saturated 0.1 M KOH. (c) Koutecky–Levich plot of Mn/Zn-N-C@30% rGO at different potential values (0.3–0.7 V). (d) CV profiles of Mn/Zn-N-C @30%rGO at 8 different scan rates in 0.1 V potential window around open circuit potential (0.1605 V). (e) Anodic and cathodic currents at OCP w.r.t different potential scans (0.005–0.8 V $s^{-1}$) of CV plotted along with linear fitting. (f) Nyquist plots of Bare electrode (magenta), Mn/Zn-N-C (green), Mn/Zn-N-C @10%rGO (blue), Mn/Zn-N-C @20%rGO (red), Mn/Zn-N-C @30%rGO (black).

The Koutecky–Levich (K–L) plot in Fig. 5.9 (c) was created using these LSV curves at a constant scan rate of 10 mV $s^{-1}$. At varying electrode potential values (0.3–0.7 V), the associated Koutecky-Levich plots ($J^{-1}$ vs $\omega^{-1/2}$) confirm good linearity, as shown in Fig. 5.9(c). With respect to the concentration of $O_2$ dissolved in solution, first-order reaction kinetics are characterised by linearity and parallelism of the graph. ORR takes place either through the 4-electron direct reduction pathway, in which $O_2$ is direct reduced to $H_2O$, or by the reduction of 2-electron pathway, in which $O_2$ is reduced to hydrogen peroxide ($H_2O_2$). The direct 4-electron mechanism is favored in ORR. The electrochemically active surface area (ECSA) of synthesized Mn/Zn-N-C@30% rGO was determined using cyclic voltammetry (CV) in an alkaline aqueous solution. CVs around the open circuit potential (OCP) of three-electrode cells at eight various potential scan rates of 0.005–0.8 $Vs^{-1}$ are depicted in Fig. 5.9(d). In order to determine the double-layer capacitance ($C_{DL}$) of a catalyst-loaded electrode surface, anodic and cathodic currents were linearly fit to the applied potential scan rates, as shown in Fig. 5.9(e). The $C_{DL}$ is calculated as the average rate of slopes of the linear fits performed to the anodic and cathodic currents. The closed polygon area under the curve of CV in an $N_2$ saturated electrolyte solution was used to determine specific capacitance (Cs). The ECSA of the electrocatalyst deposited on the surface of electrode was calculated using both $C_{DL}$ and Cs. Nyquist plots of the bare electrode and synthesized catalysts are represented in Fig. 5.9(f). Electrochemical impedance spectroscopy (EIS) is another useful method for describing the electrical conductance of catalysts in electrocatalysis. EIS of all the synthesized catalysts (Mn/Zn-N-C and Mn/Zn-N-C nanocomposites (10, 20, 30% rGO)) were calculated using the Potentiate approach with an applied voltage potential of 0.86 V by using a three-electrode system in 0.1 M KOH electrolyte. The Mn/Zn-N-C has a higher impedance than other samples and is near to the bare electrode. Mn/Zn-N-C has very high resistance, yet it does not prohibit ions and electrons from moving around in the electrolyte. The straight line might be due to ionic or electrolytic conductivity. Similarly, Mn/Zn-N-C @ 10% rGO has a lower impedance than Mn/Zn-N-C but is slightly more than other composites. The resistivity of the prepared composite was reduced by adding Mn/Zn-N-C with rGO. Resistance is reduced as the percentage of rGO in the nanocomposite increases. The semicircle in every line is imperceptible.

The ORR polarization curves of Mn/Zn-N-C @30% rGO and Pt/C commercial are shown in Figs. 5.10 (a) and 5.10 (b), respectively. After 2500 CV cycles, the Mn/Zn-N-C @30% rGO can still retrieve a significant amount of current (51%), indicating that the electrocatalyst can effectively provide current for more than 1200 cycles although maintaining a significant level of current density. While the Pt/C commercial catalyst retrieved 55% of the current, which is slightly more than the comparative catalyst. For fuel cells and several other electrochemical applications, fuel cross-over occurs on a frequent basis. In order to ensure the technical feasibility of an electrocatalyst, it is necessary to examine the durability of the material against methanol. This was accomplished by adding 0.5 M $CH_3OH$ to a solution of 0.1 M KOH. Fig. 5.10(c) shows that Pt/C is not stable in the presence of methanol, and a strong methanol oxidation peak occurs, which obscures oxygen reduction, a phenomenon known as methanol poisoning. On the other hand, there were no traces of methanol oxidation were found in Mn/Zn-N-C @30% rGO, which confirms the tolerance in methanol. The cathodic peak shows a negative shift of only 0.06 V, and a minor loss of 17% in current density of Mn/Zn-N-C @30% rGO, has been recorded by methanol.

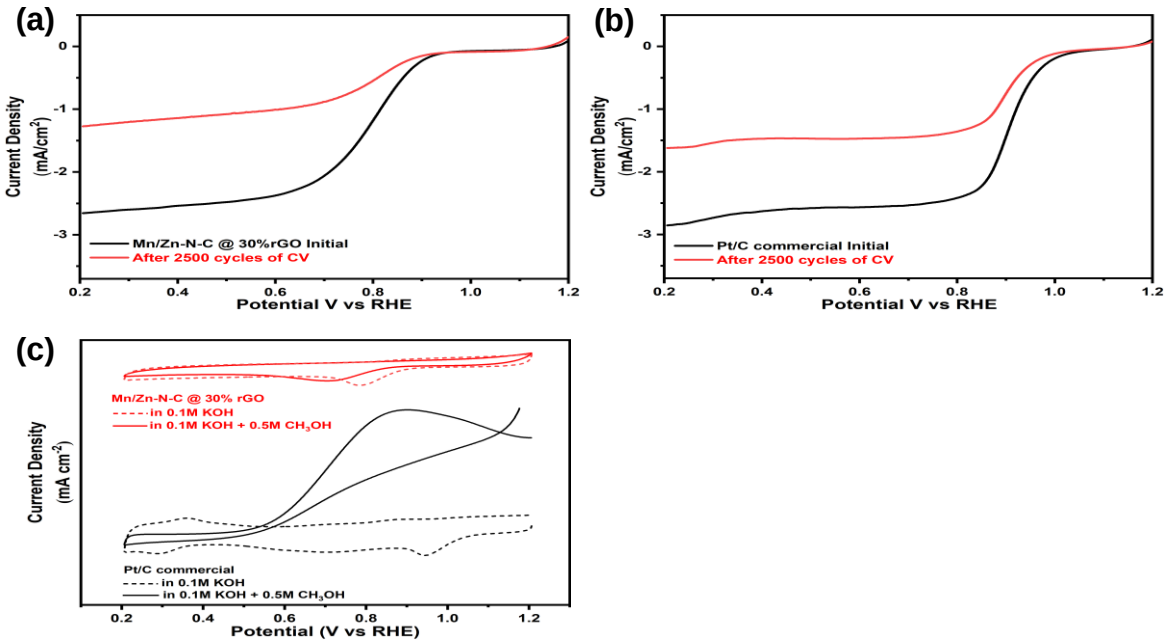


***Fig. 5.10:*** (a) ORR polarization curves of Mn/Zn-N-C @30% rGO before (black) and after 2500 cycles of CV (red). (b) ORR polarization curves of Pt/C commercial before (black) and after 2500 cycles of CV (red). (c) CV profiles of Mn/Zn-N-C @30% rGO (red) and Pt/C (black) in 0.1 M KOH (dot line) and 0.1 M KOH + 0.5 M $CH_3OH$ (continuous line) solutions.

## Summary

This chapter discusses in depth the material characterisation and electrochemical testing outcomes of synthesized electrocatalyst materials. Mn/Zn-N-C @30% rGO has shown superior electroactivity for oxygen reduction and evolution reaction among all prepared catalyst samples.

## References


[1] A. Ma, R. Zhang, "Facile synthesis of redox-responsive paclitaxel drug release platform using metal-organic frameworks (ZIF-8) for gastric cancer treatment," *Mater. Res. Express.,* 2020.

[2] A. Schejn, A. Aboulaich, L. Balan, V. Falk, J. Lalevée, G. Medjahdi, L. Aranda, K. Mozet, R. Schneider, "Cu2+-doped zeolitic imidazolate frameworks (ZIF-8): Efficient and stable catalysts for cycloadditions and condensation reactions," *Catal. Sci. Technol.,* p. 1829–1839, 2015.

[3] Y. Ye, F. Cai, C. Yan, Y. Li, G. Wang, X. Bao, "Two-step pyrolysis of ZIF-8 functionalized with ammonium ferric citrate for efficient oxygen reduction reaction," *J. Energy Chem.,* p. 1174–1180, 2017.

[4] B.D. Ossonon, D. Bélanger, "Synthesis and characterization of sulfophenyl-functionalized reduced graphene oxide sheets," *RSC Adv.,* p. 27224–27234, 2017.

[5] D. Huang, Q. Xin, Y. Ni, Y. Shuai, S. Wang, Y. Li, H. Ye, L. Lin, X. Ding, Y. Zhang, "Synergistic effects of zeolite imidazole framework@graphene oxide composites in humidified mixed matrix membranes on CO2 separation," *RSC Adv.,* p. 6099–6109, 2018.

[6] L. Yang, B. Tang, P. Wu, "Metal-organic framework-graphene oxide composites: A facile method to highly improve the proton conductivity of PEMs operated under low humidity," *J. Mater. Chem.*, p. 15838–15842, 2015.

[7] Y. Zhang, H. Niu, X. Zhang, J. Pan, Y. Dong, H. Wang, Y. Gao, "Magnetic N-containing carbon spheres derived from sustainable chitin for the selective oxidation of C-H bonds," *RSC Adv.*, p. 51831–51837, 2017.

# Chapter 6
# Conclusions and Recommendations

## 6.1 Conclusions

In this work, an electrocatalyst compound was synthesized for use as an electrocatalyst in the oxygen reduction reaction. The manganese metal organic framework (MOF) Mn-ZIF-8 was composited with graphene oxide using a simple solvothermal method that involved thermal reduction in an inert Ar-$H_2$ gas atmosphere at high temperatures. Cyclic voltammetry, linear sweep voltammetry, and electrochemical impedance spectroscopy were used to characterize the electrochemical activities of the prepared catalyst. In particular, Mn/Zn-N-C@30% rGO outperformed other nanocomposites with varying rGO contents in terms of ORR electrocatalytic activity. The electrochemical parameters of peak current density, cathodic peak potential, onset potential, half-wave potential, overpotential, Tafel slope, and methanol stability produced remarkable results. The synergistic interaction of the mesoporous, highly defective lamellar structure and the transition metal composition of MOF can be linked to notable activities of Mn/Zn-N-C@30 % rGO. The combination of polyvalent manganese metal, oxygen-deficient nanocomposite structure, and highly conductive reduced graphene oxide template provides excellent catalytic characteristics for ORR. This study presents a practical self-templated manufacturing approach for nanostructured composite synthesis that may be used to create new and novel topologies for other prospective catalytic materials with a high aptitude for electrocatalytic applications.

## 6.2 Recommendations

The major objective of this research was to discover novel materials and frameworks that could be used for energy storage. Transition metals have intrinsic polyvalent characteristics, allowing for hierarchically porous frameworks with structural, chemical, and thermal stabilities go far beyond its being expected of catalyst materials. We used a solvothermal strategy and a simple thermal reduction approach to make a manganese doped Zn-N-C @ reduced graphene oxide composite that can be used for oxygen electrocatalysis. However, the stability of current density has some downsides that need to be addressed by material control approaches. It would be strongly suggested to test these composite materials for lithium air batteries and other metal air batteries once the oxygen reduction reaction (ORR) polarization behavior is enhanced. In light of the fact that Li-air battery testing necessitates the use of a unique Swagelok type cell testing setup, it is recommended that such a setup be established in order to obtain discharge/charge cyclic performance and measure coulombic efficiencies of cells with catalyst loading in order to obtain valuable information about the performance of Li-air batteries.

# Appendix A

**Nanostructured Mn-doped Zn-N-C @reduced graphene oxide as high performing electrocatalyst for oxygen reduction reaction**

Asad Ali[1], Naseem Iqbal[1*], Tayyaba Noor[2], Umair Imtiaz[1]

[1]US-Pakistan Centre for Advanced Studies in Energy, (USPCAS-E), National University of Sciences and Technology (NUST), H-12, Islamabad 44000, Pakistan

[2]School of Chemical and Materials Engineering, (SCME), National University of Sciences and Technology (NUST), H-12, Islamabad 44000, Pakistan

*Corresponding Author: Tel: +92-51-90855281, Email: naseem@uspcase.nust.edu.pk

**Abstract**

Future fuel cells and metal-air batteries will benefit greatly from revealing self-supported electrodes with efficient oxygen reduction reaction (ORR) activity and durability. However, noble metal catalysts are expensive and unstable, necessitating research into novel metal–organic framework (MOF)-based topologies that can catalyse oxygen reduction reactions (ORR). In this work, the synthesis of nitrogen-doped carbon (N-C) is derived from zeolitic imidazolate frameworks (ZIFs) and a novel Mn-doped Zn-N-C@rGO is synthesized using a self-templated solvothermal method and their performance in an alkaline medium for oxygen reduction reaction (ORR) is studied. The nanostructured composite outperformed the commercial Pt/C catalyst in terms of both material resources and application efficacy. The Mn/Zn-N-C @30% rGO exhibit outstanding performance for ORR in KOH, with a more positive cathodic peak of 0.78 V vs RHE and an onset potential of 0.97 V vs RHE, which are characteristics that suggest the possibility of reducing ORR overpotentials. The improved electrochemical performance, small Tafel slopes and methanol tolerance are ascribed to the interdependent effect of the N-doped carbon (N-C) and the Mn/Zn active sites. Novel architecture, tunable porosities, template directed growth and remarkable electrocatalytic performance of Mn-doped Zn-N-C@rGO make it a good aspirant for energy applications.

**Keywords:** Oxygen Reduction Reaction, Metal Organic Framework (MOF), Graphene Oxide (GO)